ELSEVIER

Journal of Structural Geology 28 (2006) 1146–1166

JOURNAL OF STRUCTURAL GEOLOGY

www.elsevier.com/locate/jsg

High-resolution record of displacement accumulation on an active normal fault: implications for models of slip accumulation during repeated earthquakes

J.M. Bull [a,*], P.M. Barnes [b], G. Lamarche [b], D.J. Sanderson [c], P.A. Cowie [d], S.K. Taylor [a], J.K. Dix [a]

[a] School of Ocean and Earth Science, University of Southampton, National Oceanography Centre, Southampton SO14 3ZH, UK
[b] National Institute of Water and Atmospheric Research, 301 Evans Bay Parade, Greta Point, PO Box 14-901, Kilbirnie, Wellington, New Zealand
[c] Department of Earth Science and Engineering, Imperial College London SW7 2AZ, UK
[d] Department of GeoSciences, University of Edinburgh, West Mains Road, Edinburgh EH9 3JW, UK

Received 24 November 2005; received in revised form 28 February 2006; accepted 2 March 2006
Available online 6 May 2006

Abstract

The spatial and temporal accumulation of slip from multiple earthquake cycles on active faults is poorly understood. Here, we describe a methodology that can determine the time period of observation necessary to reliably constrain fault behaviour, using a high-resolution long-timescale (the last 17 kyr) fault displacement dataset over the Rangitaiki Fault (Whakatane Graben, New Zealand). The fault linked at ca. 300 ka BP and analysis of time periods within the last 17 kyr gives insight into steady-state behaviour for time intervals as short as ca. 2 kyr. The maximum displacement rate observed on the Rangitaiki Fault is 3.6 ± 1.1 mm yr^{-1} measured over 17 kyr. Displacement profiles of the last 9 ka of fault movement are similar to profiles showing the last 300 ka of fault movement. In contrast, profiles determined for short time intervals (2–3 kyr) are highly irregular and show points of zero displacement on the larger segments. This indicates temporal and spatial variability in incremental displacement associated with surface-rupturing slip events. There is spatial variability in slip rates along fault segments, with minima at locations of fault interaction or where fault linkage has occurred in the past. This evidence suggests that some earthquakes appear to have been confined to specific segments, whereas larger composite ruptures have involved the entire fault. The short-term variability in fault behaviour suggests that fault activity rates inferred from geodetic surveys or surface ruptures from a single earthquake may not adequately represent the longer-term activity nor reflect its future behaviour. Different magnitude events may occur along the same fault segment, with asperities preventing whole segment rupture for smaller magnitude events.

Keywords: Earthquake recurrence intervals; Fault displacement rates; Fault linkage; Normal faulting

1. Introduction

Understanding the spatial accumulation of displacement from multiple earthquake cycles on a single fault system is important for seismic hazard analysis and for determining the mechanics of earthquake rupture. Whilst surface breaks caused by historical earthquake ruptures can be identified in the field (e.g. Crone and Machette, 1984) and may give a reasonable indication of rupture dimensions, these give little information on the spatial and temporal variation in co-seismic displacement on faults. Co-seismic surface displacement correlates well with earthquake magnitude (Wells and Coppersmith, 1994; Hemphill-Haley and Weldon, 1999), although reliable measurements of surface displacement on a historical earthquake rupture are often irregularly distributed along the rupture length (see, for example, Beanland et al., 1989; Manighetti et al., 2005).

The distribution of surface displacement can be understood through inversion of teleseismic, geodetic and strong ground motion data (e.g. Wald and Heaton, 1994) or from interferometry combined with GPS data (e.g. Wright et al., 2004). Whilst these methods are broadly successful in predicting the magnitude of surface displacements, the shortness of the instrumented earthquake catalogue has meant that there has been insufficient modelling of repeated earthquakes on the same fault system.

The longer-term accumulation of displacement on faults is often modelled by assuming an idealised slip distribution for a sequence of hypothetical earthquakes (e.g. Walsh and

* Corresponding author. Fax: +44 (0)2380 593052.
E-mail address: bull@soton.ac.uk (J.M. Bull).

0191-8141/$ - see front matter © 2006 Elsevier Ltd. All rights reserved.
doi:10.1016/j.jsg.2006.03.006

Watterson, 1988; Cowie and Scholz, 1992; Peacock and Sanderson, 1996; Manighetti et al., 2005). These slip distributions are based on theoretical models for coseismic rupture which predict elliptical or triangular slip variations for each event.

Here we reconstruct the long-term accumulation of fault displacement from repeated earthquakes using seismic reflection techniques to measure offsets in marker horizons in three dimensions. We demonstrate for the first time how high frequency seismic reflection data can be used to determine the evolution of displacement on a linked active normal fault system over a long time period (15–20 kyr) using varying scales of temporal resolution, down to the distribution and magnitude of slip in single earthquakes. We use these data to assess how long a growing fault array must be observed for a reliable representation of fault activity to be gained.

We study the Rangitaiki Fault, the most active structural element of the Whakatane Graben, the offshore continuation of the Taupo Volcanic Zone, New Zealand (Figs. 1 and 2). The Whakatane Graben has a well-constrained stratigraphy based on timescales of 10^4–10^6 years, which records the development of a normal fault system that is young and active. A high fidelity record of normal fault activity over the last 17 kyr is available for the Rangitaiki Fault, with four horizons correlated from footwall to hanging-wall. The sedimentation and dip-slip rates on the faults are of the same order; and the sedimentary history contains identifiable dated horizons. Thus our study provides a much higher fidelity record than other studies of this type (e.g. Nicol et al., 2005).

2. Tectonic setting and previous work

The Taupo Volcanic Zone (TVZ; Fig. 1) is the zone of Quaternary back-arc rifting and volcanism associated with the oblique subduction of the Pacific plate beneath the Australian Plate at the Hikurangi margin. The TVZ extends northwards beneath the continental shelf in the Bay of Plenty, where the youngest rift system is the Whakatane Graben. The offshore part of the graben extends for ca. 50 km to the White Island Volcano and lies in less than 200 m water depth except for a few deeply incised canyons in the north. The bathymetric expression of the graben is a 15-km-wide subdued depression bounded by the Motuhora scarp to the east and an area of positive relief known as the Rurima Ridge on the west.

Seismicity in the Taupo Volcanic Zone is characterised by shallow (<10 km) earthquakes, with most of the earthquakes concentrated in a narrow band through the central and eastern parts of the zone. The seismic activity includes localised swarms followed by periods of relative quiescence (Bryan et al., 1999). The M_w 6.5 1987 Edgecumbe earthquake occurred under the Rangitaiki Plain, which represents the onshore part of the Whakatane Graben, close to the coast and caused 18 km of surface rupture, 7 km of which occurred on the NE striking Edgecumbe Fault, in association with 10 secondary ruptures. Average net slip of the Edgecumbe Fault at the ground surface was 1.7 m, with maximum observed vertical and extensional displacements of 2.5 and 1.8 m, respectively, producing a maximum dip-slip component of 3.1 m (Beanland et al., 1989). The focal mechanism and aftershock sequence indicate a fault dipping at $45\pm10°$ (Anderson and Webb, 1989) and rupturing to 9–10 km depth. Dislocation modelling by Beanland et al. (1990) suggested that the fault dipped at 40° to ca. 6 km depth with 2.7 m of normal slip.

Analysis of seismic reflection data within the Whakatane Graben has shown that there is widespread active normal faulting within the top 2 km of the sedimentary section (Wright, 1990; Lamarche et al., 2000; Taylor et al., 2004; Lamarche et al., in press). The graben is infilled with up to 3 km of sediments overlying an irregular, poorly defined basement, interpreted as Mesozoic greywackes with volcanic intrusions (Davey et al., 1995). Average subsidence rates of 2 mm yr^{-1} were constrained by Wright (1990) within the offshore graben, based on analysis of the post-last glacial transgressive surface that they dated at 17 ka in the Whakatane Graben. A surface extension rate of 2.9 ± 0.7 mm yr^{-1} across the graben was determined by summation of dip-slip displacement and assuming an average fault dip of 45° (Lamarche et al., in press).

Within the Whakatane graben two major faults dominate (Fig. 1): the White Island Fault bounds the eastern margin and has a clear seabed expression with a scarp (Motuhora scarp) of up to 80 m. The Rangitaiki Fault has the largest displacement across the graben on the 17 ka surface (Wright, 1990; Taylor et al., 2004). While the Rangitaiki Fault and subsidiary faults have been a fully-filled system throughout their history, determination of the history of the White Island Fault is complicated by an incomplete footwall stratigraphy. The WIF represents the boundary between dominantly dip-slip faulting in the Whakatane Graben to the west and strike-slip behaviour associated with the North Island Dextral Shear Belt.

The long-term growth history of the Rangitaiki Fault was studied by Taylor et al. (2004). They demonstrated active growth for the last 1.3 ± 0.5 Myr and documented evolution from five isolated fault segments to a fully linked fault system (Fig. 2). The Rangitaiki Fault is a typical normal fault with growth sedimentation in the hanging-wall. The maximum displacement resolved on the fault is 830 m on a 1.3-Ma-old surface (Taylor et al., 2004). Dip values calculated from depth converted sections (Taylor, 2003) show that the lowest dip within the top 2 km is 59°.

Taylor et al. (2004) showed that in the early history of fault growth the dominant process was tip propagation, with a maximum displacement rate of 0.72 ± 0.23 mm yr^{-1}. They found that interaction and linkage became more significant as the faults grew towards each other, with a fully linked fault system forming between 300 and 17 ka. An important finding of this work was that following segment linkage there was a marked increase in displacement rate, with the maximum rate averaged over 17 ka increasing to 3.4 ± 0.2 mm yr^{-1}.

Taylor et al. (2004) mainly used conventional multichannel seismic reflection data to constrain the evolution of the fault on time periods of 100s of thousands of years. In this paper we concentrate on post-linkage fault activity histories of

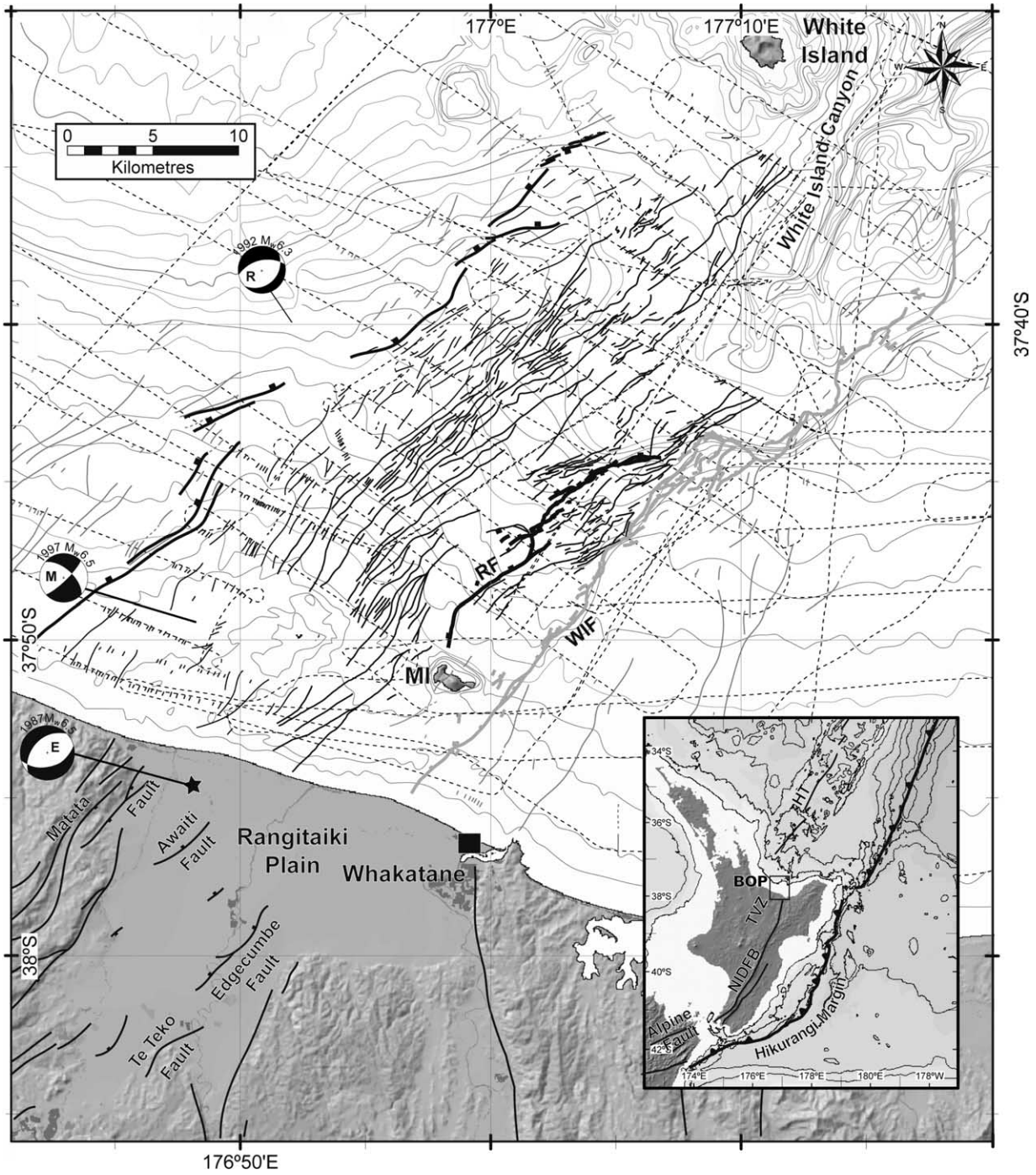

Fig. 1. Simplified structural map of the offshore Whakatane Graben and onshore digital terrain model of coastal region. The Rangitaiki Fault (RF) and White Island Fault (WIF) are highlighted. The grey dashed lines show the regional high-resolution seismic reflection data used to constrain the positions of the faults. The star represents the main shock epicentre of the M_w 6.5 earthquake (Nairn and Beanland, 1989). MI is Motuhora Island. Inset shows geodynamic environment of the North Island, New Zealand. Bathymetric contour is 500 m. NIDFB, North Island Dextral Fault Belt; HT, Havre Trough; TVZ, Taupo Volcanic Zone; BOP, Bay of Plenty. Teethed line indicates Hikurangi subduction front.

the Rangitaiki Fault on timescales of thousands of years using high-resolution seismic reflection data sets.

3. Data

Forty-six strike-perpendicular high-resolution seismic reflection boomer profiles were collected across the central section of the Rangitaiki Fault (Fig. 3), an area of 7.5×5 km, with a line spacing of between 100 and 200 m. These data form the primary data set, but extensive Chirp and 3.5 kHz data collected previously (see Lamarche et al. (2000) for a summary) were also used to aid interpretation. Whilst closely-spaced boomer data wholly constrained the central part of the fault (Fig. 2), the other data sets were used to

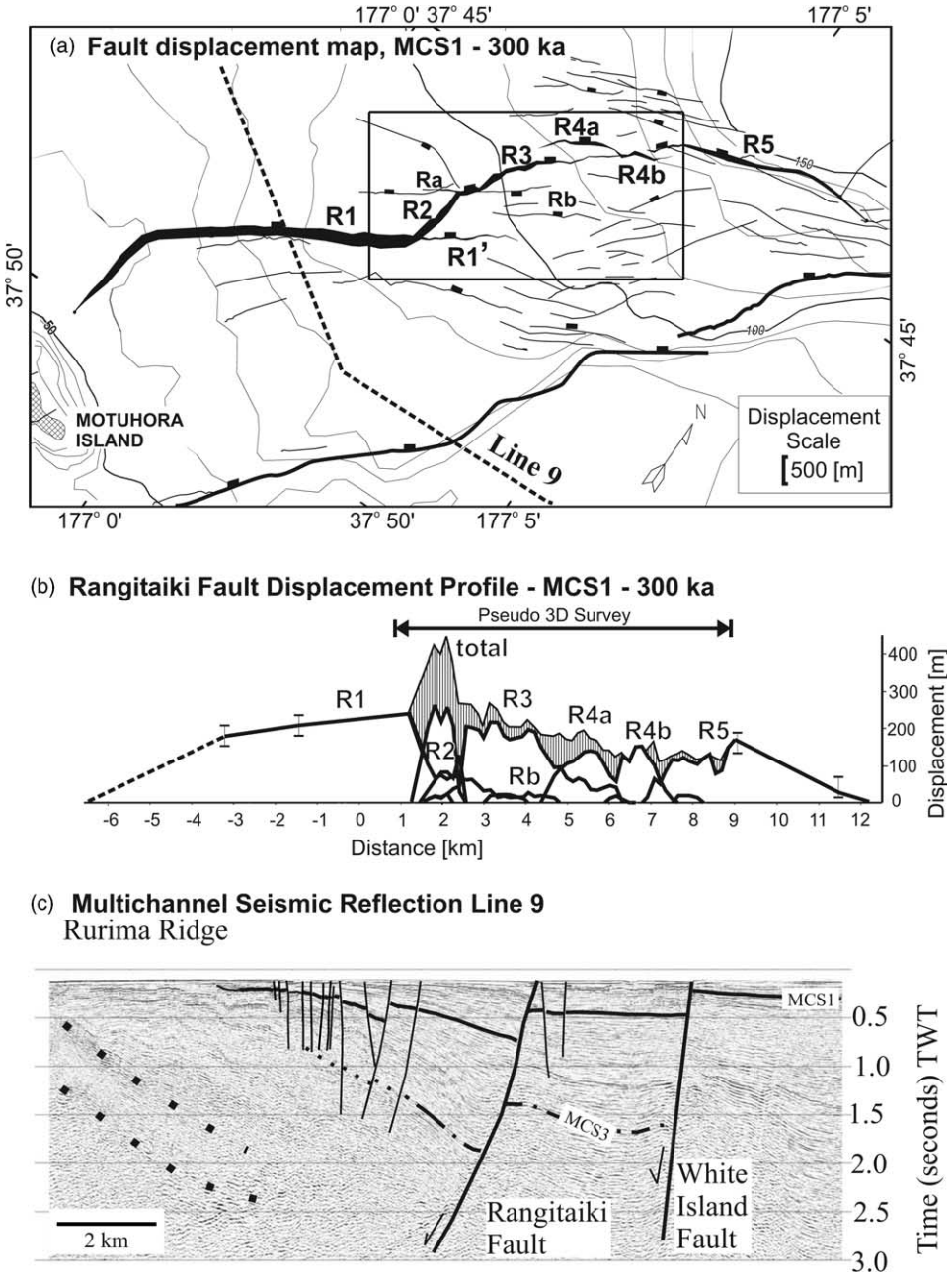

Fig. 2. (a) Map of the entire Rangitaiki Fault at horizon MCS1 (300 ± 100 ka). The main segments of the Rangitaiki Fault are numbered, the thickness of the fault represents the displacement as it varies along strike, dots show fault tips. Other faults are in thinner solid lines. Bathymetry contours are shown; there is a large surface expression of the White Island Fault. The black rectangle shows the extent of the detailed survey area, other fault displacement measurements are made from regional seismic lines for MCS1 (not shown, see Taylor et al., 2004). (b) The aggregate displacement profile for MCS1 (above hatched area in detailed survey area) for the linked Rangitaiki Fault. (c) Multichannel seismic reflection profile 9 (for position see (a)). The near-surface solid horizon is the position of MCS1 horizon 1. There are a large number of small faults on Rurima Ridge which are not shown and this fracturing makes following reflection horizons difficult onto the ridge. Vertical exaggeration is ca. 2:1.

constrain the ends of the fault. The vertical linkage of faulting was assessed using multichannel seismic reflection (MCS) data described by Taylor et al. (2004), which images the top 2 km of sediment.

The boomer profiles image the last ca. 17 ± 1 ka of sedimentation in the survey area and provide information on the top ca. 60 m of sediments. Tide and swell filtering considerably improved the clarity of seismic reflections. Subsequent to this processing, the boomer data has also been band-pass-filtered (zero-phase, corner frequencies of 300, 1000, 2500 and 3000 Hz).

Age control, for the Late Pleistocene and Holocene sediments, is provided by 43 piston cores (summarised by Kohn and Glasby, 1978; Lamarche et al., 2000). Cores were split and logged using a whole core geophysical logger and an average interval velocity of 1550 m s^{-1} was determined for the uncompacted near-surface sediments within the survey area (Taylor et al., 2004).

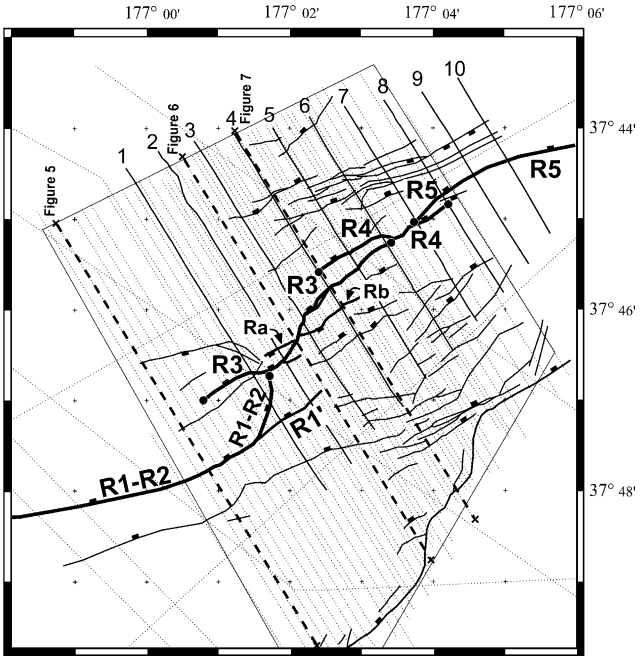

Fig. 3. Location map showing positions of boomer profiles and faults within the detailed study area covering the central part of the Rangitaiki Fault at horizon H4 (17 ka) level. The positions of 3.5 kHz profiles illustrated in Fig. 4 are illustrated (numbered 1–10), as are the positions of the boomer profiles shown in Figs. 5–7.

4. Stratigraphic framework, age control and time periods of observation

Four strong laterally continuous and easily correlated reflectors within the high-resolution seismic data (H1–H4) can be used to constrain fault evolution during the last 17 ± 1 kyr (Figs. 4–7; Table 1). Taylor et al. (2004) and Wright (1990) summarise the evidence that the near-surface 5–60-m-thick stratigraphic sequence represents the post ~17 ka transgression and these arguments will be only briefly reviewed here.

The Rangitaiki Fault trace lies at water depths of 60–100 m. At the last sea level low-stand, an incising fluvial system drained the hinterland to the south within the subsiding Whakatane Graben. H4 is the youngest regionally extensive erosion surface and probably formed in very shallow water (<20 m) at the low-stand maximum (120–140 m) and diachronously between 120 m and the coast from 17 to 6.5 ka as the zone of marine abrasion migrated with rising sea level. Given the water depths in the study area, and considering tectonic subsidence and the calibrated sea level curve of Carter et al. (1986), we estimate the age of H4 in the area relevant to this study to be 16–18 ka. Beneath H4 there are clear examples of channels, which are most likely fluvial systems that fed the canyon system to the north during the last low-stand.

Taylor et al. (2004) describe in detail the constraints on H1 given by dating of tephra (Mamaku) in sediment cores immediately above the horizon. The ages of horizons H2 and H3 were derived by Taylor et al. (2004) by using sediment thicknesses in an area away from fault zones and interpolating between the ages of H1 and H4 (see Table 1 for a summary of ages and errors).

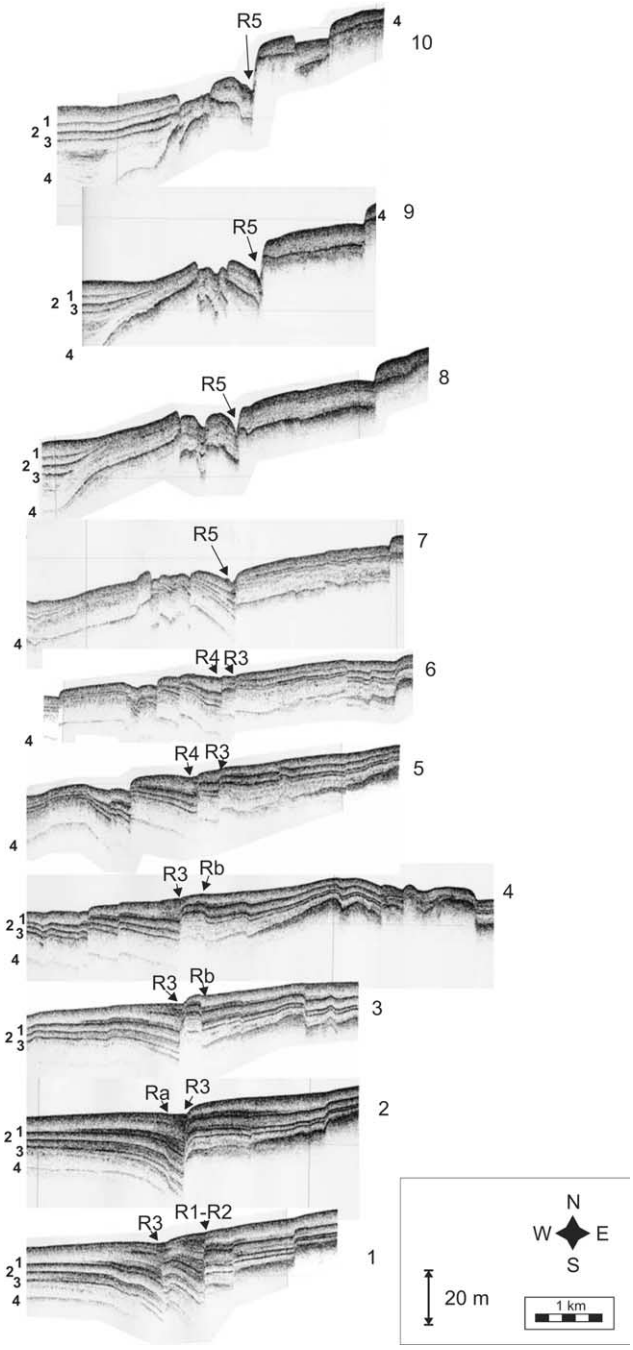

Fig. 4. Ten 3.5 kHz profiles showing the structural variation along the length of the Rangitaiki Fault. Segment numbers are indicated and profile positions indicated in Fig. 3. The position of the four horizons H1–H4 are indicated (1–4 next to each profile). Vertical exaggeration is ca. 50:1.

In the survey area, the post-glacial sediment thickens into the hanging-wall of active faults, which have very slight seabed expression. The geometry of buried sedimentary deposits shows no sign of footwall erosion, indicating that any space created by faulting was quickly infilled with sediment. Despite fairly high displacement rates,

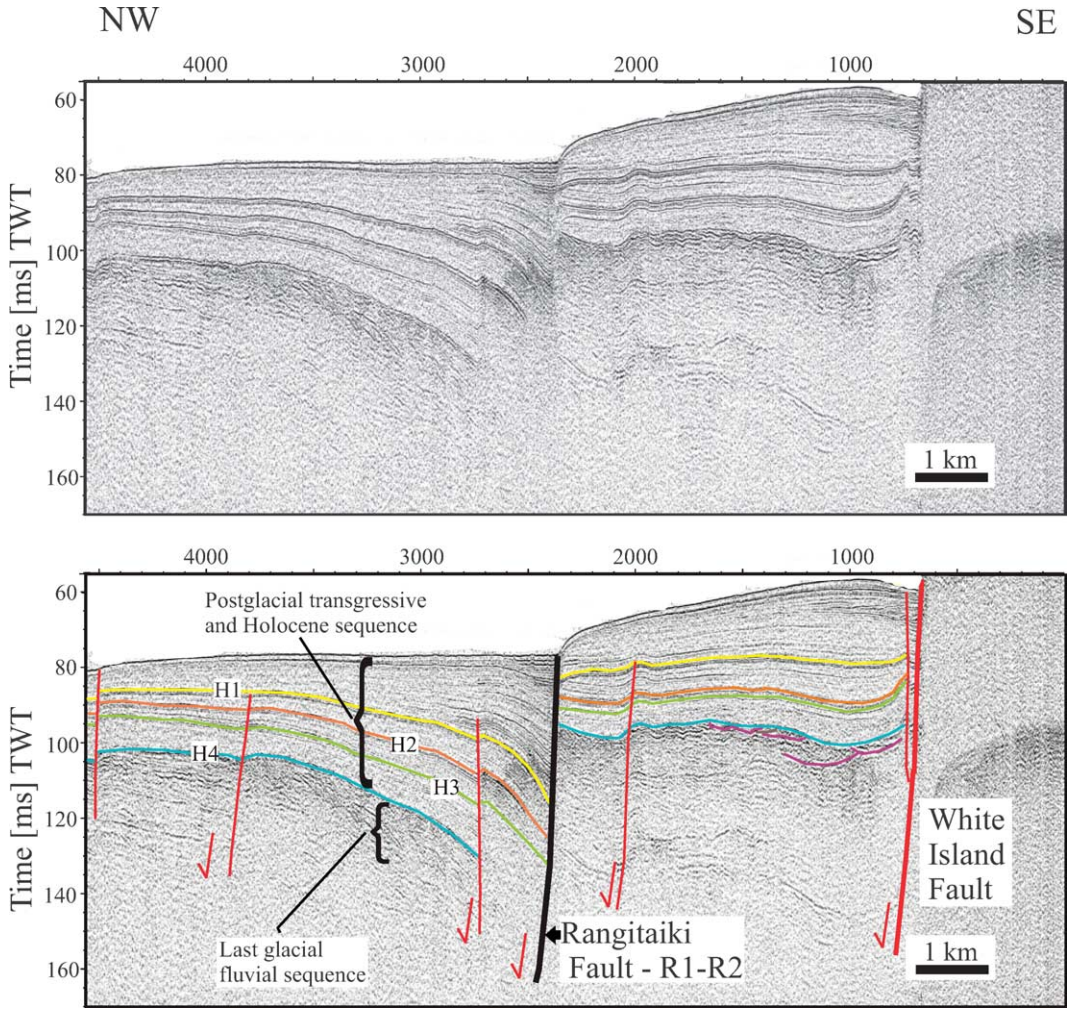

Fig. 5. Example Boomer profile illustrating the Rangitaiki and White Island faults without (above) and with (below) interpretation. The location of the profile is shown in Fig. 3. This profile images the southernmost segment (R1–R2) of the Rangitaiki Fault. Four post-glacial horizons are indicated (H1–H4) and clear growth strata are imaged in the hanging-wall of the Rangitaiki Fault. Evidence for a probable fluvial system is indicated in purple. Vertical exaggeration is ca. 65:1

a comparable rate of sedimentation has resulted in an exceptional hi-fidelity growth signature.

5. Measurements of fault displacement

The boomer data were interpreted on a 3D seismic workstation to obtain the throws (vertical separations) on all the faults. Given the steep dips (~70–80°) in the upper few tens of metres and the normal (dip-slip) nature of the faults, the throws approximate the displacement on the faults. All fault displacement diagrams in this paper are strike-projected along a N057°E axis, which corresponds to the average strike of the Rangitaiki Fault. This projection is valuable for comparing faults across strike; the *x*-axis is referred to as 'along strike' and the perpendicular *y*-axis as 'across strike'. The closely spaced seismic profiles provide excellent coverage of the structure and along-strike displacement variations of the faults.

The difference in displacement on a fault between successive horizons represents the displacement increment in the period between deposition of the two horizons. Fault displacement rates for each time period were calculated using the displacement difference between horizons and age estimates of those horizons. Errors in horizon ages are in the range 6–11%.

Errors in the measurement of displacements of the H4 horizon across the Rangitaiki Fault are derived from uncertainties in horizon picking, the interval velocities of 1550 ± 25 m s^{-1} (Taylor et al., 2004) used for calculating post-H4 sediment thickness and horizon drag observed on faults. In many cases, the largest cause of error originates from fault drag, which is a local perturbation to the displacement fields adjacent to the fault planes, in both the footwall and the hanging wall. In many cases there is fault drag adjacent to the fault planes observed in both the footwall and the hanging wall. This local perturbation to the displacement fields was corrected using the technique employed by Chapman and Meneilly (1991) and Mansfield and Cartwright (1996), whereby the horizons are projected towards the fault plane. Overall, we estimate a relative error

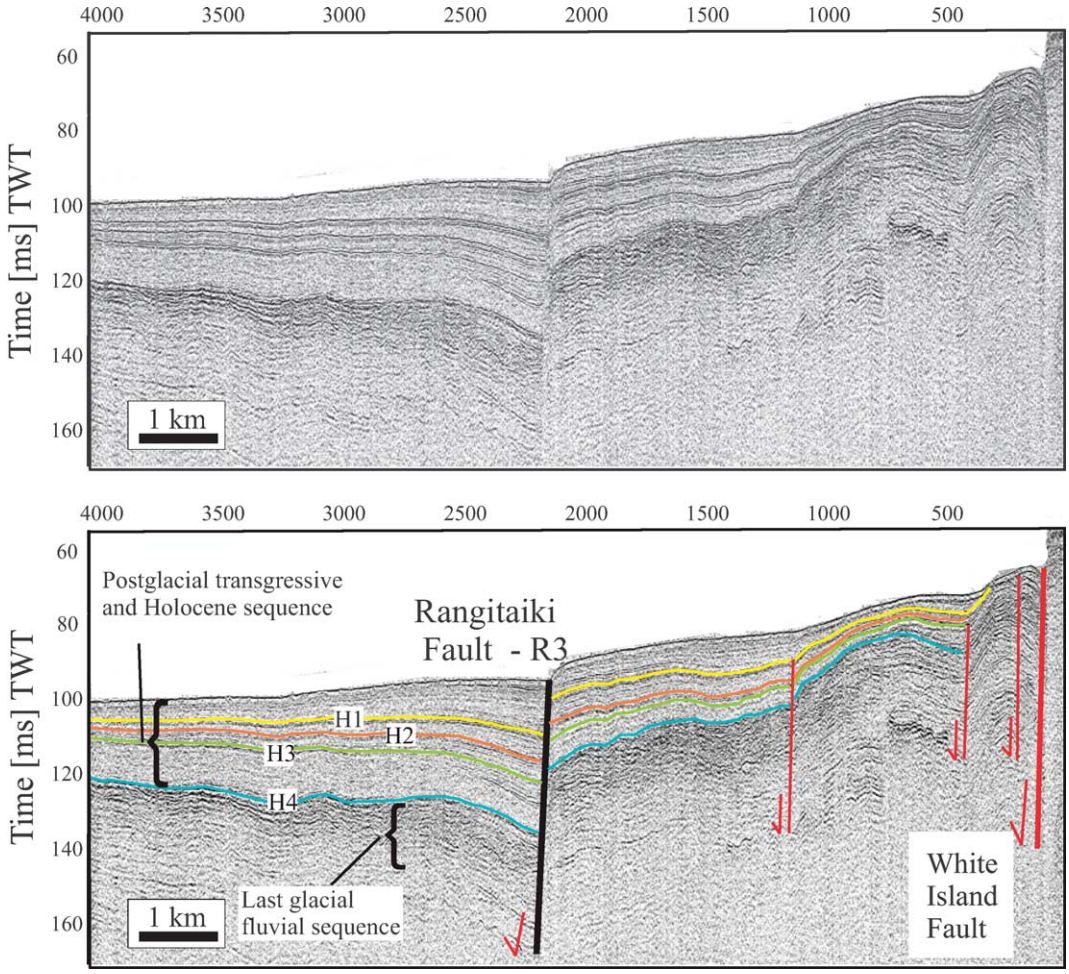

Fig. 6. Example Boomer profile illustrating the Rangitaiki and White Island Faults without (above) and with (below) interpretation. The location of the profile is shown in Fig. 3. This profile images the centre of segment (R3). Four post-glacial horizons are indicated (H1–H4) and clear growth strata are imaged in the hanging-wall of the Rangitaiki Fault. Vertical exaggeration is ca. 65:1

of 15% on displacement measurements undertaken across individual faults.

6. Results

6.1. Structural style from high resolution seismic reflection data

Ten 3.5 kHz profiles perpendicular to the strike of the Rangitaiki Fault are illustrated in Fig. 4. These profiles overlap the seismic reflection (boomer) data from the central part of the fault (Fig. 3). Examples of typical boomer data within the study area are shown in Figs. 5–7.

The profiles in Fig. 4 show the change in faulting and sedimentation along the central part of the fault. In the SW, the post-glacial sedimentary package thickens into the hanging-wall of active faults and shows only very slight surface expression of the most active faults. The four horizons, H1–H4, correlated across the survey area are readily identifiable and additional horizons are visible in the hanging-wall of the fault where the sediments are thickest. The decrease in sedimentation rate is manifest as progressively more surface expression of the faults to the northeast (see profiles 9 and 10; Fig. 4), beyond the detailed study area.

Shallow gas in the hanging-wall of the Rangitaiki Fault limits imaging of horizon H4 in the extreme southern end of the detailed survey area (Fig. 5). In all profiles there is characteristic syn-tectonic growth strata in the hanging-wall (Figs. 6–8) for all time periods constrained by the reflection data (Table 2).

6.2. Geometry of Rangitaiki Fault

The Rangitaiki Fault is approximately 20 km long and is a kinematically-linked segmented fault, with four major segments discernable from a displacement analysis over the last 17 kyr (Fig. 3; Taylor et al., 2004): R1–R2, R3, R4 and R5. Note that while segments R1 and R2 are distinct in the analysis of the 300 ka horizon (Fig. 2), in the analysis of the displacement data over the last 17 kyr they have a single displacement profile and are referred to as R1–R2. The central part of this fault was chosen as the locus for detailed study as

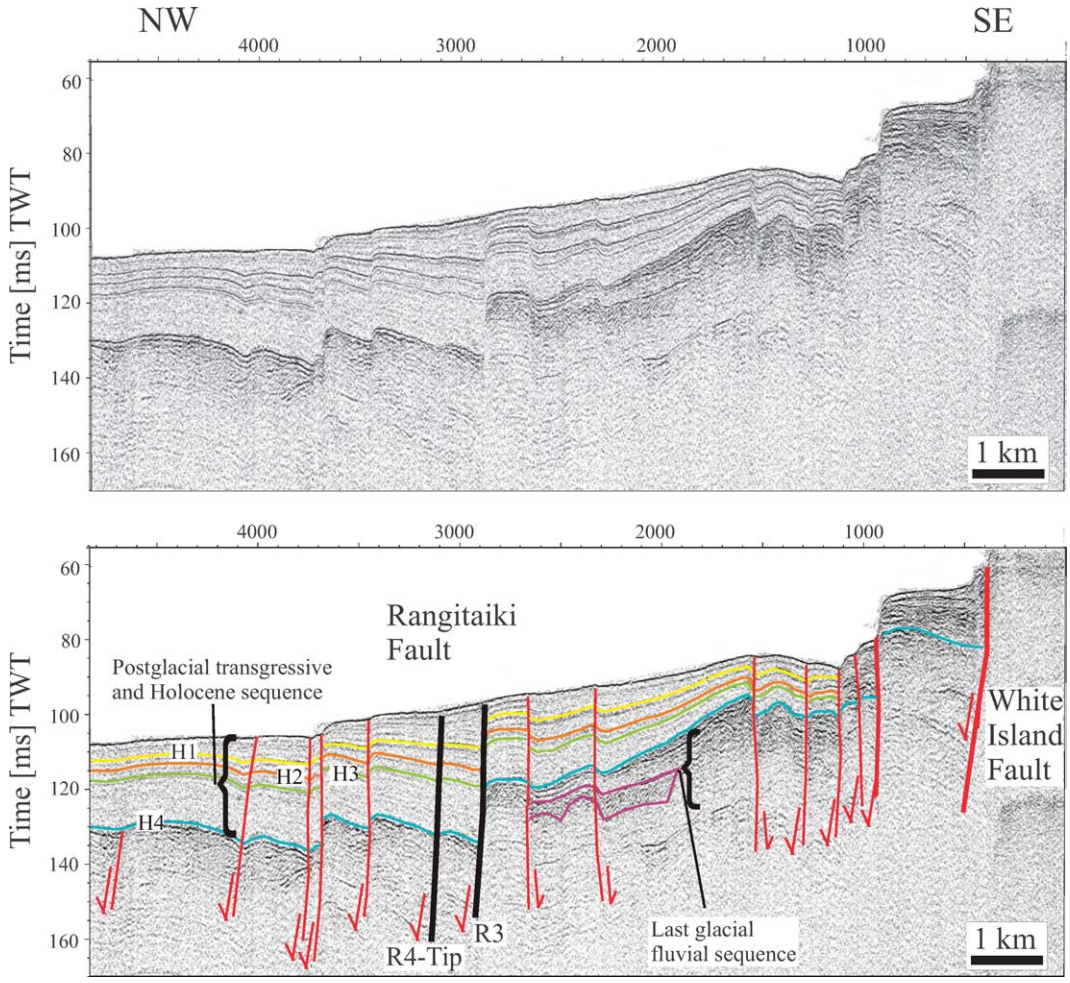

Fig. 7. Example Boomer profile illustrating the Rangitaiki and White Island Faults without (above) and with (below) interpretation. This profile images segment (R3) and the tip of another segment (R4) of the Rangitaiki Fault. Four post-glacial horizons are indicated (H1–H4) and clear growth strata are imaged in the hanging-wall of the two segments of the Rangitaiki Fault. Evidence for a probable fluvial system is indicated in purple. Vertical exaggeration is ca. 65:1.

several fault strand terminations and relays were known to be present in Pleistocene sediments allowing clear imaging of both the hanging wall and footwall fault geometries. Whilst the Rangitaiki Fault is known to dip at shallower angles in the MCS data discussed earlier (Fig. 2), in the high resolution seismic reflection data presented here dips range from 70° to sub-vertical.

The southwesternmost segment of the Rangitaiki Fault (R1–R2) is about 10 km long, accounting for approximately half the length of the entire fault, with its southern tip lying approximately 2 km north of Motuhora Island (Fig. 2). To the NE, the segments are shorter and progressively more faults are found surrounding the Rangitaiki Fault. The maximum displacement occurs near the centre of the fault system (Fig. 2b). Displacement on the Rangitaiki Fault dies out to the north in a complex zone of faulting where the Rangitaiki and White Island Faults converge.

The NE part of the southwesternmost segment of the Rangitaiki Fault (R1–R2) continued into the splay R1′ (Fig. 3). Originally R1 and R3 formed a relay ramp, but this was breached by R2 prior to 17 ka (Taylor et al., 2004). During the period 0–17 ka, R1 and R2 behaved as a single fault (R1–R2) with a continuous displacement gradient to a tip at the NE end (Fig. 9).

R3, R4 and R5 have strike-lengths of 5, 4 and 4 km, respectively, and behave as a system of left-stepping, overlapping fault segments whose tips are clearly defined (Figs. 3 and 9). R1–R2 links to R3 and the two segments overlap by 1.7 km. R3 also intersects R4, about half-way along its length and the two segments overlap by 4 km. R4 and R5 form an unbreached relay ramp with an overlap of ~300 m.

Table 1
Ages of near-surface seismic horizons in the Whakatane Graben (from Taylor et al., 2004)

Horizon	Age (ka)
H1	9.0±1
H2	11.4±1
H3	13.9±1
H4	17.0±1

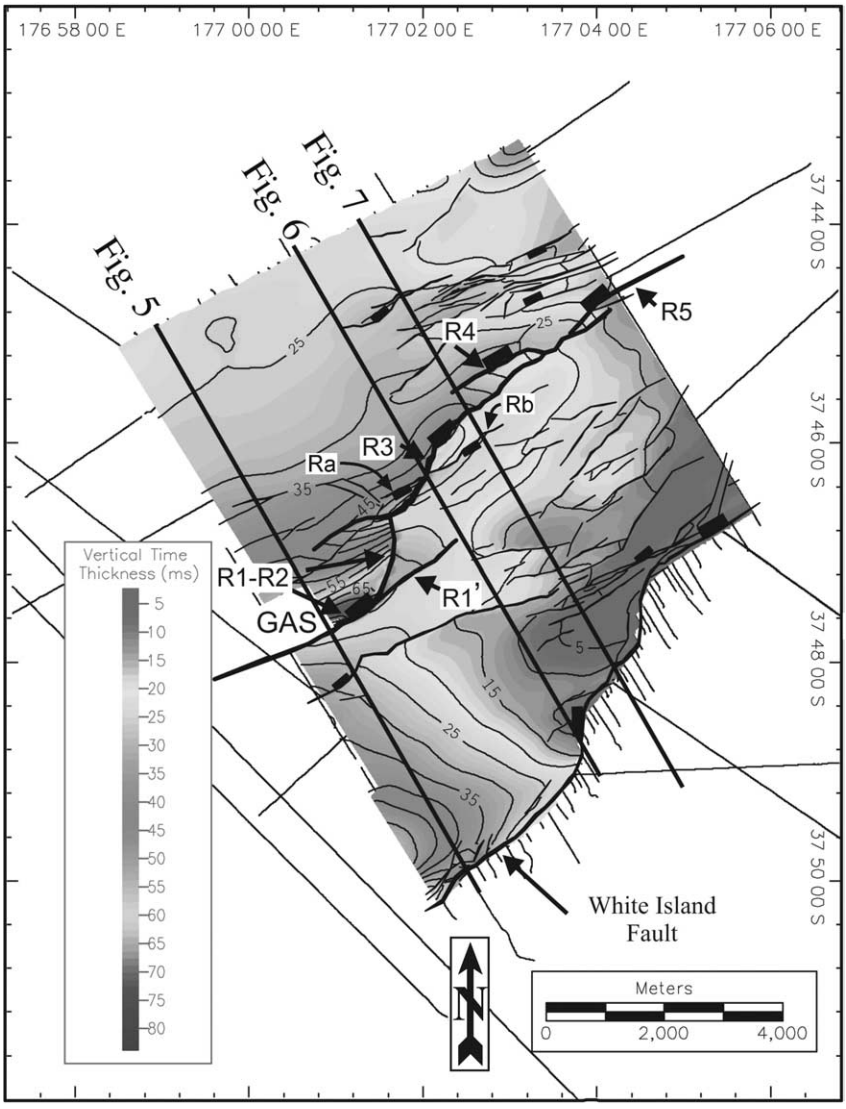

Fig. 8. Fault and isopach map of sediments deposited since H4 (over 17 kyr) around the central section of the Rangitaiki Fault, derived from the high-resolution seismic reflection data shown in Fig. 3. The four segments of the Rangitaiki Fault (R1–R2, R3, R4 and R5) are shown with clear sediment depocentres in their hanging walls. The positions of the profiles shown in Figs. 5–7 are shown.

Thus, in geometrical terms, the fault traces of R1–R2 and R3 are linked, as are the traces of R3 and R4. On the other hand, segments R4 and R5 form a simple relay, i.e. they are not geometrically linked, but displacement is transferred between the two segments. In any discussion of segment linkage it is useful to distinguish carefully between geometrical linkage (where the fault surfaces and fault traces are joined through intersection or abutment) and kinematic linkage (where there are systematic or continuous variations in the displacement on the segments, indicating some form of displacement transfer across the linkage). In the past, linkages have been described as hard-linked (where the faults are geometrically, and usually kinematically, linked) and soft-linked (where the faults are geometrically unlinked, but usually kinematically, linked) (Walsh and Watterson, 1991). In this paper, we will distinguish geometrical and kinematic linkage of faults. Two faults are geometrically linked (G_L) if their surfaces intersect at a given horizon (i.e. their traces on this horizon intersect), otherwise they are geometrically unlinked (G_U). Two faults are considered to be

Table 2
The 10 time periods constrained by horizons H1–H4

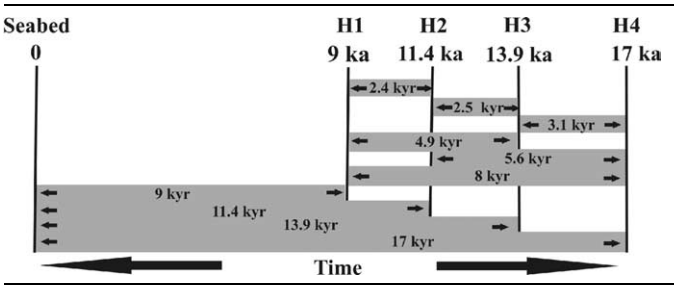

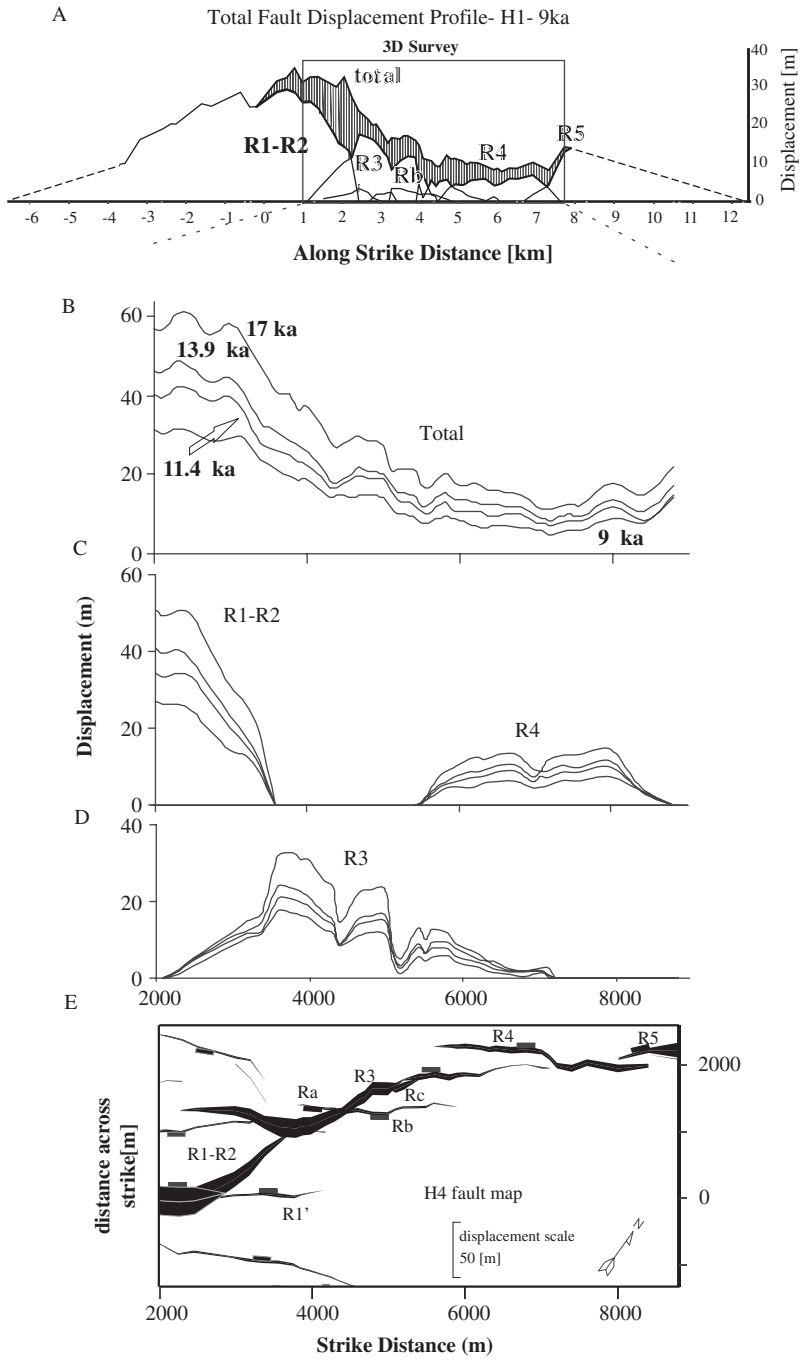

Fig. 9. (A) Fault displacement profile along the entire Rangitaiki Fault for the 9 ka horizon. (B) Displacement accumulation on the entire Rangitaiki Fault system from the 9, 11.4, 13.9 and 17 ka horizons within the detailed study area. (C) As (B) but for segments R1–R2 and R4. (D) As (B) but for segment R3 only. (E) Map showing fault displacements of the 17 ka horizon (H4) and the positions of the major segments. The width of the fault legend is proportional to the displacement on the horizon (see scale).

kinematically linked (K_L) if their displacement profiles show a simple continuous variation from one-to-another, be partially linked (K_P) is there is some systematic relationship, often with a displacement low, as is common in relay ramps, or unlinked (K_U) if their displacement profiles are unrelated. The characteristics of the linkage of segments of the Rangitaiki Fault are summarised in Table 3.

In addition to the major segments, the Rangitaiki Fault includes some smaller fault segments. Faults Ra and Rb down-throw to the southeast (antithetic to the main segments of the Rangitaiki Fault) and intersect segment R3 at 4200 m along strike (Fig. 3). Rc is a small splay, completely attached to R3, and while visible in the high resolution data is not resolvable in the MCS data.

Although the Rangitaiki Fault system is a kinematically-linked structure, its segmented nature is still clear from the isopach map of the post-glacial sediment (Fig. 8), where the contours show several separate depocentres near the centres of

Table 3
Summary of fault segments and types of linkage on the Rangitaiki Fault in the period 0–17 ka. G_L—geometrically linked; K_L—kinematically linked; K_P—partially linked; $G_{L/U}$—uncertainty whether geometrically unlinked or linked

Fault	Segment type	Fault	Linkage
R1	Long single segment	R1	
			G_L K_L
R2	Branch splay from R1	R2	
			G_L K_P
R3	3 sub-segments with variable linkage	R3	
			$G_{L/U}$ K_P
R4	2 sub-segments, single fault since 17 ka	R4	
			G_U K_P
R5	Single segment	R5	

the fault segments, marking the locations of high displacement and increased sediment accommodation space. Note that the main depocentre occurs at the link between R1 and R2, supporting the idea that these acted as a single fault (R1–R2) over, at least, the last 17 ka.

Throughout the post-glacial sedimentary sequence (between H4 and the seabed) there is no observed lateral fault propagation. However, the minimum distance of 100 m between adjacent profiles means that only lateral propagation rates of more than 6 mm yr^{-1} would be resolvable.

6.3. Fault displacements on the Rangitaiki Fault system

At horizon H4 (17 ka), the displacement on the Rangitaiki Fault decreases fairly steadily from a maximum of 62 m near the centre of the linked fault network (~2500 m along strike; Fig. 9b) to ~15 m on R4 (at 7500 m along strike; Fig. 9b). The NE half of the fault comprises major segments that are kinematically linked producing a displacement gradient of $\sim 8 \times 10^{-3}$ for the 17 ka horizon.

Fig. 9 shows the accumulation of displacement with time on individual segments within the detailed study area and how this contributes to the total displacement profile. The displacement-distance variation of segments R3 and R4 on all four horizons is completely constrained. To the north and south of the detailed study area the 11.4, 13.9 and 17 ka horizons are less well resolved and the displacement distribution along the entire Rangitaiki Fault is known for only the 9 ka horizon.

There is a notch in the displacement profile of R3 at its intersection with Ra and Rb (e.g. Fig. 10a); the sum of displacements on Ra and Rb at the intersection point is the same as the difference between the observed notched profile and a projected smoothed profile for R3. Fault Rc is a small splay fault in R3, with maximum displacement of 12 m at 5200 m along strike on horizon H4. The displacement of Rc is complimentary to a notch in the displacement profile of R3 (Fig. 10a).

6.4. Fault displacement history

The same fault segments (R1–R2, R3, R4 and R5) are present throughout the post-glacial sequence and show no resolvable lateral propagation. By comparing the displacement over different time intervals (Fig. 10) the displacement history of the fault segments can be examined. Fig. 10 shows the displacement differences over time intervals: A (17 ka–present); B (17–13.9 ka); C (13.9–11.4 ka); D (11.4–9 ka); and E (9 ka–present). Knowledge of the time intervals between these horizons allows the displacement rates to be calculated (Fig. 11).

The aggregate displacement curve (grey lines in Fig. 10) is fairly smooth on timescales greater than 9 kyr (Fig. 10A and E; see also Fig. 2), whereas for shorter time intervals of 2–3 kyr (e.g. Fig. 10B–D), the profiles are much more irregular, with large differences in displacement rate being observed over different time intervals and where the segments intersect and/or interact. The aggregate displacement lows seen on the Rangitaiki Fault segments at short timescales are not compensated by activity on other faults (for example faults in the footwall and hanging-wall) (Taylor, 2003).

The variations in displacement accumulation are described with reference to four key locations (1–4; see Fig. 10 for locations) along the strike of the fault.

6.4.1. Location 1—Overlapping tips of R1–R2 and R3

In the post-glacial sediment sequence, segments R1–R2 and R3 overlap by 2 km and are spatially separated by 1 km (Fig. 10F), with the tip of R1–R2 just intersecting R3 at location 1. The maximum displacement is at the intersection of R1 and R2 at 2900 m along strike (Fig. 10A), where R1 continues to the NE on R1′, with a much reduced throw (<20% of that on R1–R2). Over the entire interval 0–17 ka, the displacement gradient across location 1 is smooth, as displacement is transferred from R1–R2 to R3.

6.4.2. Location 2—R3 crossed by antithetic faults Ra and Rb

At location 2, the segment R3 intersects with two antithetic fault segments, Ra and Rb, which may have formerly been the same fault (Fig. 10F). Throughout the last 17 ka, the summed throws on these faults has remained fairly constant. If heave is proportional to throw (i.e. constant dip) then this suggests that these faults accommodate a fairly constant extension rate at this location and that R3, Ra and Rb are kinematically linked. The opposite sense of downthrow on Ra and Rb will reduce the net throw on the fault system at location 2, as is clearly seen in the isopach map (Fig. 8).

Examination of Figs. 10 and 11 indicates variation in the displacement and displacement rates over different time intervals. Between 17 and 13.9 ka (Fig. 10B), the displacement profile of R3 shows a notch at the intersection point, with the drop in displacement being equal to the sum of the displacements on Ra and Rb at this point. During the 13.9–9 ka period (Fig. 10C and D), R3 is effectively pinned at the intersection point, with no displacement accumulation for the 4000 year duration. During the 13.9–11.4 ka interval (Fig. 10C), Ra has the highest displacement rate of 0.33 mm yr^{-1} at the intersection point, whereas in interval 11.4–9 ka (Fig. 10D), the displacement on Rb is high, with the displacement on Ra being zero. During interval 9–0 ka (Fig. 10E), R3 is reactivated at the intersection point and

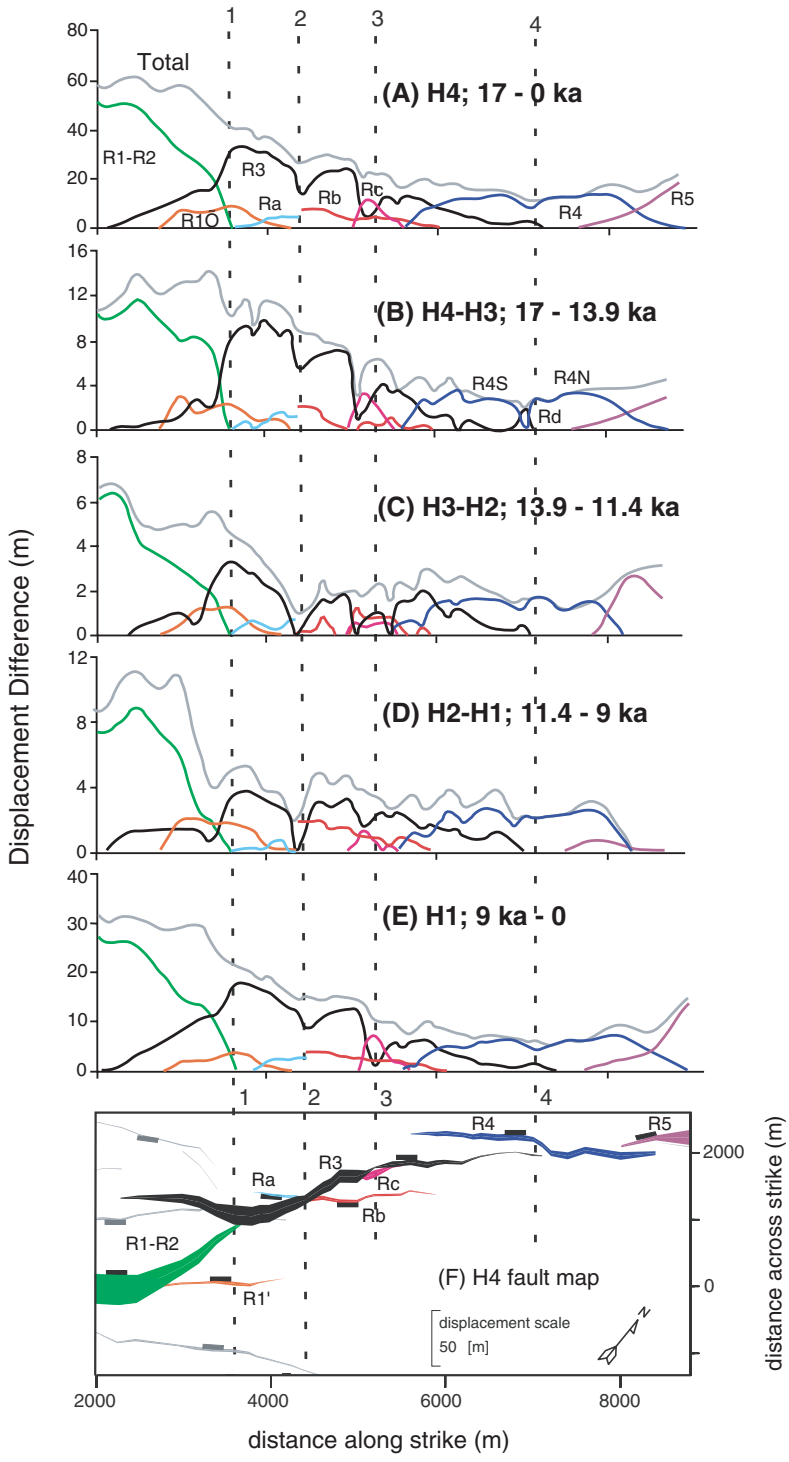

Fig. 10. Profiles of total displacement on the Rangitaiki fault for different time periods ((A)–(E)). (F) Displacement map for horizon H4. The main segments of the Rangitaiki Fault are named and in colour; the thick grey line shows the aggregate displacement profile for each time period. Segment R1–R2 continues south of the detailed study area (see Fig. 2) but is not well imaged at the H2–H4 levels on the high-resolution data.

both Ra and Rb have similar displacement profiles increasing from their tips towards the intersection point.

6.4.3. Location 3—Rc splay from R3

At 5200 m along strike, the displacement on the Rangitaiki Fault is divided between R3, Rb and Rc, with the aggregate displacement maintained across location 3 at different time periods by different relative contributions of the three faults (Fig. 10). The displacement profile of Rc almost exactly matches a notch in the displacement profile of R3; this relationship is most clearly seen in the longer time intervals (Fig. 10A and E).

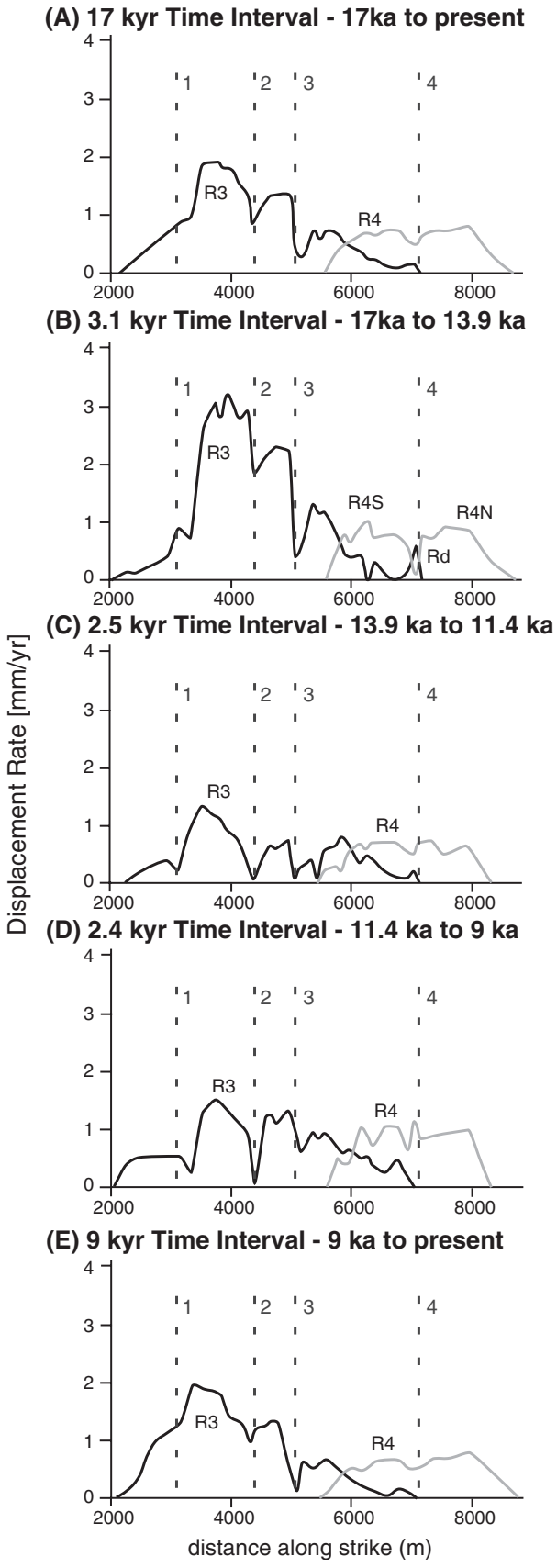

Fig. 11. Displacement rate variations along segments R3 (black) and segment R4 (grey) for different time periods. The positions of four locations of fault interaction are indicated (see Fig. 10F).

6.4.4. Location 4—Tip of R3 intersecting centre of R4

The intersection of R3 and R4 (7100 m along strike; Fig. 10F) shows a variety of configurations. During interval 17–13.9 ka (Fig. 10B), R4 appear to be acting as two sub-segments (R4N and R4S) that intersect at location 4. The tip of fault R3 also shows a localised displacement high at this point (Rd; Fig. 10B), possibly representing a separate segment with a maximum slip rate of 0.46 mm yr^{-1} (Fig. 11B). There is only a small drop in the R4 aggregate displacement profiles at location 4 (Fig. 11A–E), suggesting that the faults are kinematically linked at this location. During the 13.9–11.4 ka interval (Fig. 10C) the NE tip of R3 (Rd) shows a similar isolated high in displacement rate of 0.23 mm yr^{-1}, with a similar drop in the profile of R4. From 11.4 to 0 ka (intervals D and E; Figs. 10 and 11), the whole of R4 shows a continuous displacement profile, suggesting that it acted as a single fault, with displacement on R3 extending to meet R4 at location 4, incorporating Rd.

6.4.5. Summary

The displacement variations seen for the interacting fault segments at these four locations indicate some general features:

1. The complex system of fault segments maintains a fairly continuous displacement gradient, suggesting that the Rangitaiki Fault is behaving as a kinematically coherent system. The varying segments at its NE end maintain an overall symmetrical displacement profile similar to the single fault (R1) at its SW end.
2. Linkage between fault segments is achieved by tip-to-fault linkage (as R3 to R4), in places with clear development of branching splays (e.g. R2 branching from R1 to link to R3).
3. There is considerable variation in the displacement distribution at different time intervals. Some fault segments (e.g. R1 and R2 and the sub-segments of R4) establish geometrical linkage (G_L) and then behave as a single fault kinematically (K_L). Others (e.g. R1–R2 and R3, and R3, Ra and Rb) maintain displacement variations (K_U and K_P) throughout the 0–17 ka period despite being geometrically linked (G_L).
4. Variation in the displacement distribution occurs over time and is most obvious for the shorter time intervals (see next section).

6.5. Variations of locus of displacement and displacement rate over different time periods

Table 4 summarises the variation in average aggregate displacement rate and maximum aggregate displacement rate for different time periods for the entire Rangitaiki Fault. Over the last 17 ka the average rate (total slip divided by number of observations) along the Rangitaiki Fault was 1.7 ± 0.5 mm yr^{-1}, while the maximum rate was 3.6 ± 1.1 mm yr^{-1}. For shorter time periods there is variation around these values, but the variation is within the estimated errors. Slip rates range from 1.1. to 2.2 mm yr^{-1} (Table 4) for individual time periods,

Table 4
Average and maximum displacement rates for the Rangitaiki Fault for different time periods. The calculation of average displacement rates for the entire fault system was determined by summing the aggregate strike-projected displacement rates and dividing by the number of observations (line crossings)

Time period	Average rate mm yr^{-1}	Maximum rate mm yr^{-1}
17–0 ka	1.7 ± 0.5	3.6 ± 1.1
17–13.9 ka	2.2 ± 1.4	4.5 ± 2.9
13.9–11.4 ka	1.1 ± 0.8	2.7 ± 2.2
11.4–9 ka	2.0 ± 1.5	4.6 ± 3.8
9–0 ka	1.8 ± 0.5	3.5 ± 1.1

with an average of these values giving 1.7 ± 0.5 mm yr^{-1}, so that the spatially averaged slip rates on the Rangitaiki Fault appear to have been constant over time periods from 2 to 17 kyr.

However, from the previous section it is evident that the detailed fault segment geometry controls the distribution of displacement and this is variable on different timescales. Table 2 shows the 10 different timescales of observation over which displacement accumulation can be determined from the data. The displacement and slip rate variations for each time period for segments R3 and R4 are summarised in Table 5.

In order to illustrate the variability of spatially averaged slip rate over different time periods, Fig. 11 shows displacement rate variations along segments R3 and R4. Segments R3 and R4 were chosen for detailed study because they are completely contained within the detailed study area. Fig. 11 shows that the effects of relict segment boundaries (locations 1–4) can be seen on all time periods of observation. However, these affects are most clearly seen on the shortest time periods of 2–3 kyr. The displacement profiles for the shorter time periods (17–13.9, 13.9–11.4 and 11.4–9 ka; Fig. 11B–D) are more irregular, with zero displacement rates recorded at some points on the profiles.

Quantification of this temporal and spatial variability in slip rate was studied using a two-part process. Firstly the slip rate along the segment was normalised by the mean slip rate (Table 5) for each respective interval for all possible 10 time intervals within the data. This analysis resulted in the 10 curves that are represented by symbols in Fig. 12. Normalisation by mean slip rate is more representative than using the maximum for irregular distributions. Fig. 12 shows that the mean normalised slip rate profiles for all time periods (solid lines in Fig. 12) are almost identical to the longer time periods (compare with the shape of profiles in Fig. 11; 17 ka–present; 9 ka–present). Individual values are also plotted to assess scatter about the mean and it is clear that where the mean normalised slip rate is a minima there is considerably greater scatter. This scatter is due to the fact that these minima correspond to areas of fault interaction, where for some short time intervals there is no slip. This is particularly noticeable at location 2 on segment R3 (Fig. 11C (13.9–11.4 ka) and D (11.4–9 ka)) where there are some time periods with much lower slip rates than the longer-term averages (Fig. 11A). This deficit is recovered in another short time period (17–13.9 ka) where there are higher slip rates (Fig. 11B).

The second stage in the quantification of the temporal variability of slip rate is to find the residuals between the normalised mean slip rates in Fig. 12 and the 17 ka–present normalised mean slip rate (the longest time period of observation in this data set). The variance of these residuals was then plotted against the length of the time period of observation (Fig. 13). This allows quantification of the difference in shape between the shorter timescale slip rate profiles and that determined from the longest fault activity history. The variance decreases with increasing length of time period (Fig. 13). The temporal variability in slip rate for segment R4 is lower, as reflected in the generally lower values

Table 5
Displacement and slip rate summary for segments R3 and R4 for 10 different time periods

Segment	Time interval (ka)	Duration of interval (kyr)	D_{max} (m)	D_{mean} (m)	Spatially averaged slip rate (mm yr^{-1})
R3	17–present	17	32.7	13.9	0.82
R3	13.9–present	13.9	24.0	10.52	0.76
R3	11.4–present	11.4	20.7	9.29	0.81
R3	17–13.9	3.1	9.8	3.7	1.19
R3	13.9–11.4	2.5	3.3	1.2	0.48
R3	11.4–9	2.4	3.7	1.8	0.75
R3	9–present	9	17.6	7.2	0.80
R3	17–9	8	15.3	6.7	0.84
R3	17–11.4	5.6	12.1	4.9	0.88
R3	13.9–9	4.9	6.5	3.0	0.61
R4	17–present	17	13.9	9.8	0.58
R4	13.9–present	13.9	10.0	7.6	0.55
R4	11.4–present	11.4	8.4	6.4	0.56
R4	17–13.9	3.1	3.2	2.3	0.74
R4	13.9–11.4	2.5	1.6	1.1	0.44
R4	11.4–9	2.4	2.7	1.7	0.71
R4	9–present	9	7.1	4.7	0.52
R4	17–9	8	7.2	5.5	0.68
R4	17–11.4	5.6	4.8	3.4	0.61
R4	13.9–9	4.9	4.1	3.1	0.63

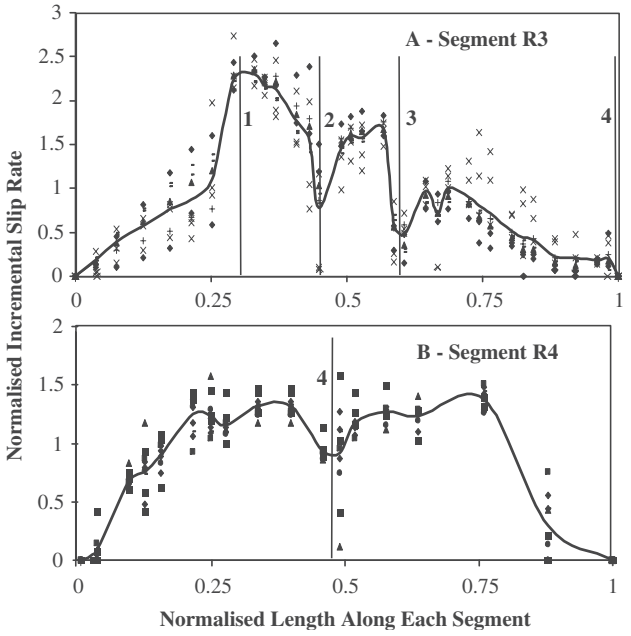

Fig. 12. Graph of normalised incremental slip rate against normalised length for (A) segment R3 and (B) segment R4. This figure was produced by normalising the mean slip rate for each of the 10 time intervals in Table 2 while segment length was normalised by total length. The solid line shows the normalised mean slip rate for all time intervals. The symbols show the normalised incremental slip rate for each time interval. The vertical lines numbered 1–4 represent locations shown in Fig. 10F.

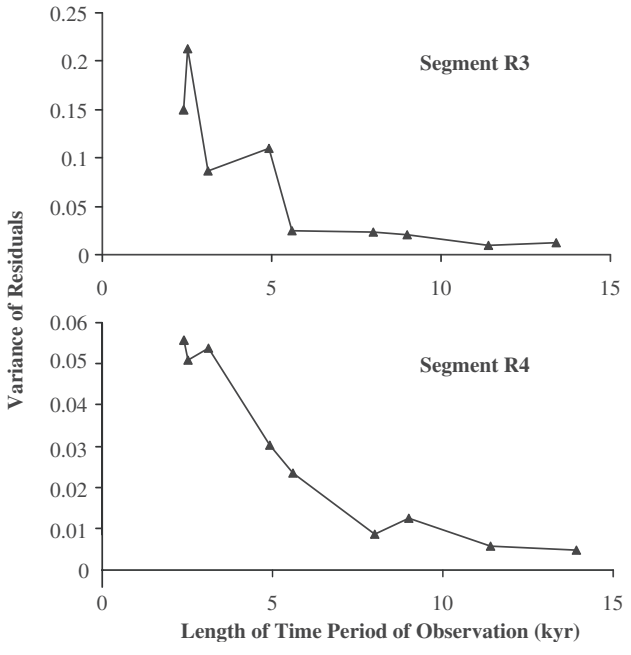

Fig. 13. Analysis of the variation in the displacement profile for time periods less than 17 kyr compared with the 17 kyr displacement profile for (top) segment R3 and (bottom) segment R4. This was calculated by first determining the residual between each of the normalised displacement profiles shown in Fig. 12 and the normalised displacement profile for the longest time period of observation (17 kyr). The variance in the residuals was then plotted against the time period of observation.

of the variance, as would be expected. An interesting result is that the variance declines rapidly and for both segments is essentially constant for time periods longer than 5.6 kyr.

In summary, the shape of the slip rate profiles along individual segments of a fault system is similar for timescales of observation of longer than 6 kyr. Slip rate profiles determined from shorter fault activity histories are likely to be more variable and reveal slip complexity related to fault interaction at fault tips.

6.6. Summary of results

In the previous sections (Sections 6.1–6.5) it has been shown that analysis of the boomer seismic reflection data within the detailed study area has allowed complete analysis of the displacement history of two segments of the Rangitaiki Fault (R3 and R4) over the last 17 kyr. The main findings are:

1. There is no observable evidence for lateral propagation of fault segments, consistent with linkage at 300 ka as described by Taylor et al. (2004).
2. Both segments show pronounced displacement minima where there are fault intersections and/or interactions with other structures: for R3 these are where an antithetic fault cross-cuts and where there is a splay; for R4, where the tip of R3 meets the middle of the segment.
3. Spatially averaged slip rate along the Rangitaiki Fault has been constant through the last 17 kyr.
4. There is considerable slip rate variability along each segment with maxima values occurring where there are no interactions with neighbouring faults.
5. Slip rates at displacement minima along R3 and R4 are variable depending on the time period and length of time period of observation. In some short time periods of observation there is no displacement accumulation at some points along segment R3, while during other time intervals it has a higher than average rate of slip.
6. An analysis of variance showed that the shape of the slip rate profile is stable for time periods of observation longer than 6 kyr.

7. Discussion

7.1. Spatial and temporal variability in slip rate

These data illustrate that slip rate varies along a fault segment and that there is temporal variability of slip rate particularly at displacement minima where fault segments interact. We believe the displacement profiles determined from our data (Fig. 10) are uniquely reliable and on the shorter timescales the displacement accumulated on the studied fault likely reflects no more than a few earthquake events (see below). Overall we argue that the evolution of the displacement profiles is controlled by the history of fault linkage and interaction.

The observation that there are points of zero displacement along segment R3 on some short time periods (13.9–11.4 and

11.4–9 ka; Fig. 10) shows that displacement on this segment has accumulated through a series of slip events that did not rupture the entire length of the fault plane. Between 13.9–11.4 and 11.4–9 ka there was no displacement at locations 2 and 3, where an antithetic fault intersected a segment or where a splay linked into the main segment. In other comparable time periods (17–13.9 ka) displacement accumulation at these sites implies different earthquake scenarios, involving through-going ruptures along the entire length of segment R3. The locations where the fault geometry is at times a barrier to fault slip (locations 2–4) creates displacement lows that are not compensated for by development of, or increased activity on, surrounding faults.

Thus, on timescales of 2–3 kyr, two key observations can be made. First, individual segments may or may not rupture along their entire length. Second, the entire fault system may have displacement deficits or surpluses along its length relative to the stable longer-term distribution. This implies that displacement data determined from surface ruptures on timescales of less than 2 kyr on this fault system would not give representative estimates of individual segment or whole fault array earthquake potential.

7.2. Earthquake rupture scenarios, recurrence intervals, and coseismic displacements

Growth in the hanging-wall of the Rangitaiki Fault is recorded by the seismic reflection data for all the 10 time intervals (Table 2) defined by our data over the last 17 kyr. This implies that at least one ground-rupturing earthquake on the fault occurred within each time interval, whilst the above displacement analysis indicates that surface ruptures, and perhaps earthquake magnitudes, have not been regular.

In the absence of direct paleoseismic information, we calculated the moment magnitudes (M_w) associated with a range of earthquake rupture scenarios and crustal fault geometry (Table 6), using the empirical relationship of Wells and Coppersmith (1994):

$$M_w = 3.93(\pm 0.23) + 1.02(\pm 0.1)\log(A)$$

where A is the rupture area. The rupture scenarios include a range of possible rupture depths from 6 to 10 km, a planar fault with a range of possible average fault dips in the crust (40–60°; Lamarche et al., in press) and a range of individual and composite rupture segmentation. The rupture segmentation scenarios include the individual surface segments recognised, an entire fault rupture, as well as other composite segment scenarios considering the locations of the displacement pinning points identified above.

From the empirical estimates of moment magnitude, we determined the seismic moment (M_o) for each rupture scenario, using the relationship of Hanks and Kanamori (1979), relating magnitude and seismic moment, whereby $\log M_o = 1.5M_w + 16.1$ (Table 6). Earthquake recurrence intervals (RI) were then estimated using two methods. First, we divided the average coseismic displacement, D, by the slip rate, S, i.e. $RI = D/S$, whereby $D = M_o/\mu A$, with μ the crustal rigidity of 3×10^{11} dyne cm^{-2}. Second, we divided the seismic moment by the moment rate ($RI = M_o/M_{orate}$, where $M_{orate} = \mu AS$ (Wesnousky, 1986)).

Table 6 shows moment magnitudes of M_w 5.4–5.8 would be associated with earthquakes limited to the smallest individual segments of 4 km length (R4 and R5). Considering the very low implied length to width (down-dip extent) aspect ratios of 0.25–0.50 for these segments, and a likely threshold magnitude for surface rupture of about M_w 5.8 in the Taupo Volcanic Zone (Villamor and Berryman, 2001), it is very unlikely that ground-rupturing earthquakes would be limited to these individual segments, so this is an unrealistic rupture scenario. Considering the displacement anomaly across the step-over between R3 and R4 (Fig. 11) and the fact that the slip rate and aggregate displacement since 17 ka increase northward from R4 to R5, it is conceivable that segments R4 and R5 have at times ruptured together in events of about M_w 5.7–6.0 (Table 6).

Earthquakes associated with rupture of the remainder of the fault south of R4, involving combined segments R1–R2 and R3, would have maximum magnitudes of M_w 5.9–6.3. The magnitudes associated with the above scenarios vary slightly for similar rupture scenarios pinned at the impediments identified near the centre of R3 (Table 6). It is also possible, considering the displacement anomalies observed at each end of segment R3, that R3 has, at times, ruptured on its own; however, considering the segment length to width aspect ratio of 0.3–0.7, we consider this unlikely. In comparison, earthquakes rupturing the entire 19 km fault would have magnitude M_w 6.1–6.5, comparable with the M_w 6.5 1987 Edgecumbe Earthquake on land, which ruptured a total fault length of about 16–18 km (Anderson et al., 1990).

The recurrence intervals for various rupture scenarios, derived from the two empirical methods described above, are presented in Table 6. These intervals for all earthquake scenarios are of the order of 100–300 years. These short return times reflect the moderate seismic moments combined with high slip rate. The estimates of coseismic displacement averaged over the fault surface, D, derived from the seismic moment, range from 0.2 to 0.7 m.

The M_w 6.5 1987 Edgecumbe Earthquake produced maximum surface dip-slip displacement of 3.1 m on the Edgecumbe Fault (Fig. 1) (Beanland et al., 1990). A dislocation model incorporating geodetic measurements and a 13 km rupture to 6.4 km depth indicated normal slip of about 2.7 m (Darby, 1989). Beanland et al. (1990) showed that surface displacements of >1.0 m were limited to about 25% ($\sim$4 km) of the fault trace and that the average surface displacement over the entire 16 km of surface rupture was about 0.9 m. This value compares well with empirical estimates of displacement averaged over the fault surface, D, of about 0.5–0.6 m, when using a comparable range of earthquake source parameters as for the Rangitaiki Fault (Table 6). By analogy with the Edgecumbe Earthquake, we can infer that maximum surface displacements associated with large earthquakes on the Rangitaiki Fault could be up to 3 m.

Table 6
Rupture parameters and estimates of maximum moment magnitude (M_w) and recurrence intervals (RI) for segments and composite scenario along the Rangitaiki Fault

Index	L (km)	α[a] (°)	H[b] (km)	W[c] (km)	L/W[d]	A[e] (km^2)	M_w[f]	M_o[g] dyne cm	D[h] (m)	S_{max}[i] (mm yr^{-1})	RI-1[j] (years)	RI-2[k] (years)
R1–R2 (min)	9.0	60	6	7	1.3	62	5.8	5.51E+24	0.29	3.50	80	80
R1–R2 (max)	9.0	40	10	16	0.6	140	6.1	1.90E+25	0.45	3.50	120	130
R3 (min)	5.0	60	6	7	0.7	35	5.5	2.24E+24	0.22	1.90	110	110
R3 (max)	5.0	40	10	16	0.3	78	5.9	7.73E+24	0.33	1.90	170	170
R4 (min)	4.0	60	6	7	0.6	28	5.4	1.59E+24	0.19	0.80	230	240
R4 (max)	4.0	40	10	16	0.3	62	5.8	5.49E+24	0.29	0.80	360	370
R5 (min)	4.0	60	6	7	0.6	28	5.4	1.59E+24	0.19	1.50	120	130
R5 (max)	4.0	40	10	16	0.3	62	5.8	5.49E+24	0.29	1.50	190	200
All (min)	19.0	60	6	7	2.7	132	6.1	1.73E+25	0.44	3.60	120	120
All (max)	19.0	40	10	16	1.2	296	6.5	5.96E+25	0.67	3.60	180	190
Composite scenarios												
R1–R2+0.5×R3[l]	10.5	60	6	7	1.5	73	5.8	6.98E+24	0.32	3.60	80	90
R1–R2+0.5×R3[l]	10.5	40	10	16	0.7	163	6.2	2.40E+25	0.49	3.60	130	140
R1–R2+R3	12.5	60	6	7	1.8	87	5.9	9.11E+24	0.35	3.60	90	100
R1–R2+R3	12.5	40	10	16	0.8	194	6.3	3.14E+25	0.54	3.60	170	180
0.5×R3[l]+R4+R5	9.0	60	6	7	1.3	62	5.8	5.51E+24	0.29	1.50	190	200
0.5×R3[l]+R4+R5	9.0	40	10	16	0.6	140	6.1	1.90E+25	0.45	1.50	300	300
R4+R5	7.0	60	6	7	1.0	48	5.6	3.75E+24	0.26	1.50	170	170
R4+R5	7.0	40	10	16	0.4	109	6.0	1.29E+25	0.40	1.50	260	260
Edgecumbe[m]	16.0	60	6	7	2.3	111	6.0	1.33E+25	0.40			
Edgecumbe[m]	16.0	40	10	16	1.0	249	6.4	4.58E+25	0.61			
Edgecumbe[n]	16.0	45	8	11	1.4	181	6.5	6.14E+25	0.90			

[a] Fault dip.
[b] Minimum and maximum depths to base of the seismogenic zone.
[c] Width (down-dip extent) $W=\alpha/\sin(H)$.
[d] Length to width shape ratio $=L/W$.
[e] Area $A=W*L$.
[f] $M_w=3.93\pm0.23+1.02(\pm0.1)\log(A)$; from Wells and Coppersmith (1994).
[g] Calculated from $\log(M_o)=16.1+1.5M_w$; from Hanks and Kanamori (1979).
[h] Single event displacement calculated from $M_o=\mu AD$, where earth rigidity modulus $\mu=3\times10^{11}$ dyne cm^{-2}.
[i] Maximum slip rate over the last 17 kyr (see Table 4).
[j] Recurrence interval calculated using $RI=D/S_{max}$; rounded up to the nearest multiple of 10.
[k] Recurrence interval calculated using $RI=M_o/M_{orate}$ (Wesnousky, 1986) with $M_{orate}=\mu AS_{max}$; S_{max} in cm yr^{-1}; rounded up to the nearest multiple of 10.
[l] Constrained by displacement pinning point L2 (see text).
[m] M_w, M_o, D calculated using L from Beanland et al. (1990); α from Lamarche et al. (in press).
[n] M_w and M_o calculated using L and H from Anderson et al. (1990). D is average observed surface displacement from Beanland et al. (1990), i.e. not calculated as above.

Beanland et al. (1989) identified at least two additional faulting events in the last 1850 years B.P, from trenches excavated across the Edgecumbe Fault. The earliest event is uncertain, but was tentatively proposed to be around 1850 years B.P., while a later event occurred around 800 years B.P. These data imply a minimum recurrence interval of about 800–>1000 years. These longer recurrence intervals are consistent with estimates of recurrence intervals for the Rangitaiki Fault based on maximum displacement arguments. The displacement value derived in Table 6 (column 10, derived via the seismic moment estimate) is the average displacement over the whole fault plane, not the maximum surface or sub-surface displacement. Hence the shorter average recurrence intervals derived in Table 6 are due to the use of the average displacement. In all likelihood, the true average return time will vary between the short intervals in Table 6 (100–400 years) and the longer return time of ca. 1000 years predicted from the maximum displacement.

The fact that we observe growth strata in the shortest time intervals (Table 2) of 2400, 2500 and 3100 years on the Rangitaiki Fault (Fig. 11) is consistent with the estimated recurrence intervals (Table 6) and the preceding discussion. Between 11.4 and 9 ka, segment R3 had a maximum displacement of 3.3 m irregularly distributed over its 7.3 km length. Between 13.9 and 11.4 ka, segment R3 had a maximum displacement of 3.1 m, while segment R4 had a maximum displacement of 1.6 m. From the above discussion, these displacements could be explained by a single ground-rupturing earthquake if associated with the larger magnitude scenarios, i.e. with rupture occurring along several segments. Alternatively, the displacements may have accrued from the lower-displacement tips of larger composite ruptures (e.g. R1–R2–R3, R4–R5), or from several smaller earthquakes.

In contrast, during the period 17–13.9 ka, the mean slip rate on R3, 1.2 mm yr^{-1}, was the highest of any time interval (Table 5; Fig. 11B) and a maximum displacement of 9.8 m accumulated in 3.1 kyr. Whilst displacement along R3 was accumulated irregularly during this period, the large displacement at location 2 ($\sim$5.6 m, $\sim$1.8 mm yr^{-1}) and continuity of displacement accumulation from 0 to 5000 m along strike indicates that earthquake ruptures involving R3 were not arrested at location 2 during this period.

Looking at the entire time frame resolved in our data, the average displacement on the Rangitaiki Fault over the last 17 kyr is $\sim$29 m (which is around 50% of the maximum displacement). Dividing the average total displacement by the maximum slip of 3 m that can be expected during the larger composite earthquakes, implies a minimum of about 10 large events on the fault.

7.3. Implications for models of slip accumulation during repeated earthquakes

Several earthquake models have been proposed for slip distribution and recurrence behaviour on segmented active faults (Schwartz and Coppersmith, 1984). The characteristic earthquake model assumes that the rupture length, magnitude and distribution of slip from a 'characteristic event' along a particular fault segment is repeated in successive events. Hence for any point along the fault segment the incremental steps in displacement are approximately constant. Furthermore when repeated characteristic earthquakes occur, the slip distribution will vary along the length of the segment, with largest co-seismic slip where the highest long-term displacement occurs and lowest displacement near segment boundaries (Schwartz, 1989). In contrast the uniform slip model (Schwartz and Coppersmith, 1984) implies constant slip rate and displacement per event at a given site, with relatively large earthquakes interspersed with frequent moderate events that contribute to smoothing out the aggregate displacement profile. In the variable slip model (Schwartz and Coppersmith, 1984), there is variation in earthquake size, displacement per event and rupture location.

In this study we are able to directly evaluate these models and determine which one best describes the displacement accumulation over multiple earthquake cycles. The 17 kyr displacement profile of the Rangitaiki Fault indicates two areas of preferential displacement; the largest centred on the overlap between segment R1–R2 and R3 and the second on R5 (Fig. 10A). This pattern closely matches that on an older horizon estimated to be about 300 kyr old (Taylor et al., 2004) (Fig. 2B). From our data on segments R3 and R4 we suggest that the slip distribution along at least these segments is not constant and depends on the time frame of observation. At short time scales, displacement distribution is irregular. However, over longer timescales the slip distribution geometry becomes stable.

Inverse models of earthquakes show that slip can be extremely heterogeneous, both along strike and down-dip (for example the Landers earthquake (Wald and Heaton, 1994) and the Denali earthquake (Wright et al., 2004)). The variability of the sub-surface slip distribution is thought to reflect 'asperities' on the fault plane at seismogenic depths. This spatial heterogeneity in the slip is inferred not only from inverse modelling, but also in surface offset data (e.g. Beanland et al., 1989; Sieh et al., 1993). Hence short timescale variability shown in these data for the Rangitaiki Fault could be reflecting variability over the entire fault plane.

It is possible to use the displacement data shown in Fig. 9 to back-strip and determine the accumulation of slip during different periods for individual segments and this is shown for R3 in Fig. 14A. The displacement lows along the segment correspond to the locations of fault interaction previously discussed. Although the displacement that accrued during each interval, and the cumulative slip along the segment, go to zero at the segment tips, this may not reflect the end of the zone of earthquake rupture along the fault. The analysis of rupture parameters for single segments, composite segment rupture and whole fault failure given in Table 6 suggests that isolated segment rupture is generally unlikely. We suggest that the pinning points on R3 were barriers to different composite ruptures that variously involved R1–R2, R4 and R5, and parts

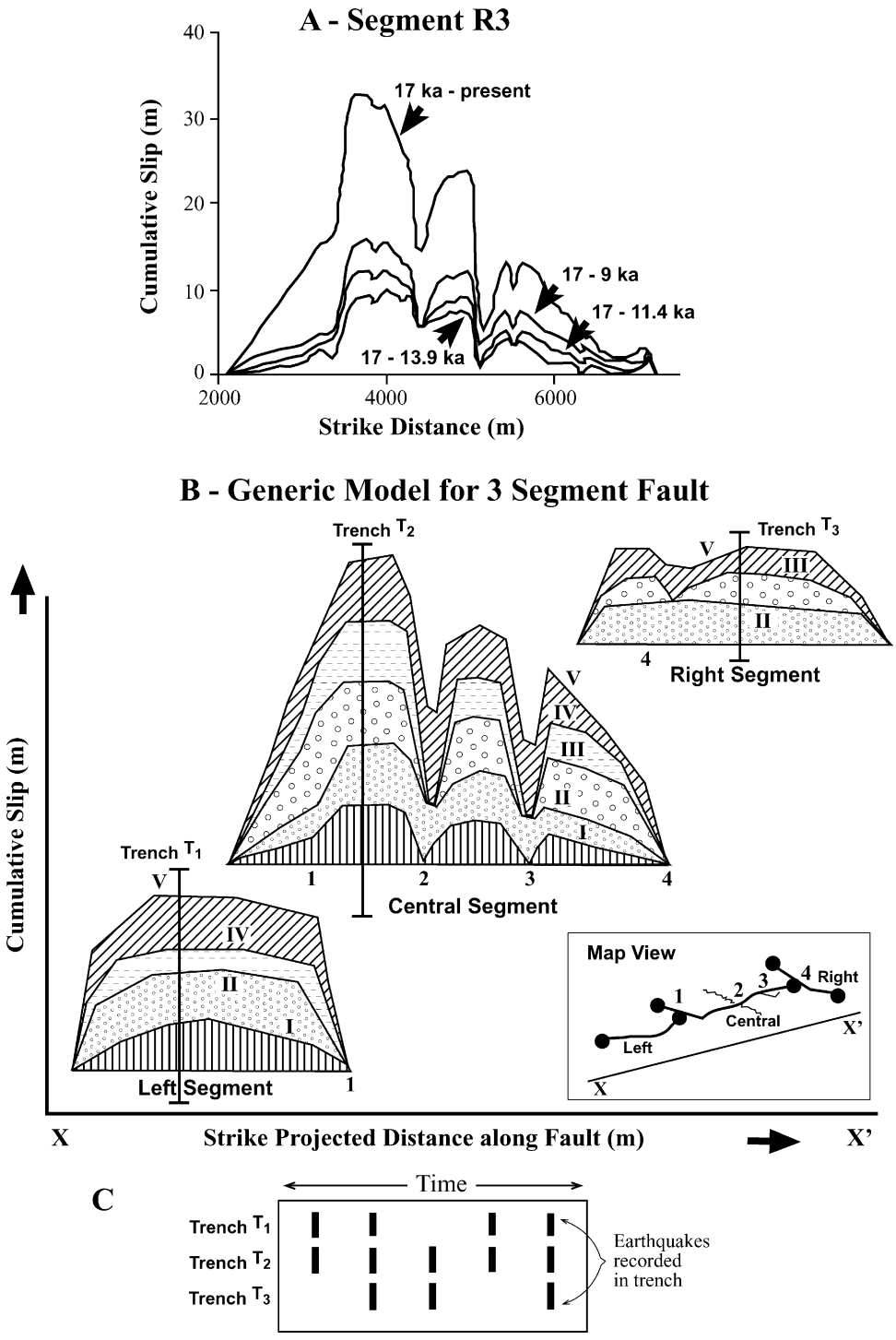

Fig. 14. Slip accumulation on Segment R3 and a generic model. (A) Slip accumulation on R3 determined by back-stripping the displacement data illustrated in Fig. 9. (B) Generic model of a three-segment fault that could produce the observed slip accumulation. The cumulative slip after five earthquakes (I–V) is shown along the fault. Note that this is a model of steady-state behaviour (the fault has fully linked prior to any of the earthquakes shown). Earthquakes I, III and IV do not rupture the entire fault plane but rupture two of the three segments and displacement is also pinned where a antithetic fault crosses the main fault (position 2) and where there is a small splay from the main fault (position 3). Earthquakes II and V rupture the entire fault plane. The inset shows a map with the main fault segments (end points denoted by circles) and minor faults highlighting fault interactions in the model. The positions of three hypothetical trench sites are also indicated (T1–T3) and information on earthquakes recorded is shown in (C).

of R3. In different earthquakes the sections of surface rupture may have jumped around, involving R1–R2–R3, R3–R4–R5 (or parts of R3), R4–R5, or just R1–R2. It is conceivable that even just R3 may have ruptured, as a whole segment. It is also likely that rupture along the whole Rangitaiki Fault occurred with all segments failing in an event similar to the Edgecumbe earthquake. This undoubtedly shows that many earthquake cycles have built up the total displacement profile.

Fig. 14B shows a generic cartoon of the accumulation of earthquake slip suggested by our data. The cartoon shows the accumulation of slip after a three-segment fault has become fully linked. The inset map shows the fault system with locations of fault interactions numbered. Some earthquakes (II and V in Fig. 14) rupture the entire fault and variable amounts of slip are accumulated along strike. At other times (earthquakes I, III and IV) only two of the three segments ruptured with locations of segment interactions variously impeding the propagation of the earthquake rupture. The important point here is that the fault growth and earthquake behaviour has been variable in time. This has resulted in spatial and temporal variability in slip accumulation within some single segments, within short time intervals (~2–3 kyrs in the case of the Rangitaiki Fault, i.e. approaching the return times of one or a few earthquakes). The fault behaviour clearly does not support a simple characteristic earthquake model, but some characteristic type events may occur episodically. The data shows that on occasions earthquake ruptures have been limited to only parts of the fault network, whilst ruptures of the entire fault, associated with the larger magnitudes, are also extremely likely on occasions and may be consistent with the characteristic model. The aggregate displacement profile is the sum of the variability associated with many earthquake cycles.

The advantage of fully spatially sampling the fault system in comparison with trenching studies is examined in Fig. 14C. The positions of three hypothetical trench sites are shown, one crossing each segment. While the trench sites reliably record earthquake occurrence on each segment, there is unlikely to be information on lateral variability in displacement, or on the role of fault interaction in controlling displacement accumulation on each segment.

Aki (1984) similarly describes two families of earthquakes associated with activity at Volcano Usu in Japan. One of these families of earthquakes exhibited consistent recurrence intervals and slip, ruptured the entire fault plane and is consistent with the characteristic earthquake model (Schwartz and Coppersmith, 1984). The other family of earthquakes shared the same fault plane, but exhibited varying amounts of slip. Aki (1984) suggests that this latter family may be explained by the presence of weak barriers along the fault plane, whereas strong stable barriers to rupture propagation persist through many earthquakes. The complexity of fault geometry influences the propagation of earthquake ruptures because of the formation of structural heterogeneity that resists rupture propagation. We suggest that our slip data for the last 17 kyrs is consistent with the observation of Aki (1984). The larger magnitude events, or characteristic events, which rupture the entire segment over longer timescales (>6 kyr for segment R3), dominate the slip distribution.

These observations highlight that the time frame of observation is of critical consideration when considering fault system behaviour. If the time frame is much longer than the recurrence interval of large earthquakes (greater than 6 kyr for the Rangitaiki Fault; Fig. 13), then the total displacement distribution (or range-front uplift) may be representative only of the largest earthquakes. However if the time frame of observation is of the same order as the recurrence interval of any ground-rupturing earthquakes, or if the only data available on a fault are surface displacement observations associated with one or two coseismic events, then the observed slip distribution (or uplift) may be unreliable for predicting long-term earthquake behaviour on the fault.

8. Conclusions

We demonstrate that the application of marine high-resolution seismic reflection data to an area with a constrained stratigraphy has the potential to resolve the history of displacement accumulation on active faults on timescales that will shed light on cycles of earthquake activity. A method for determining the length of time period of observation necessary to reliably record fault system behaviour is explained and applied to the Rangitaiki Fault.

1. Displacement profiles of the last 9 kyr of fault movement are regular and similar to profiles showing the last 300 kyr of fault movement. In contrast, profiles determined for short time intervals (2–3 kyr) on two of the fault segments are highly irregular and show points of zero displacement within the larger segments. This indicates temporal and spatial variability in incremental displacement associated with ground-rupturing earthquakes. Some earthquakes appear to have been confined to specific segments, whereas larger composite ruptures have involved the entire fault.
2. The aggregate displacement profile of the entire Rangitaiki Fault represents the sum of the variability associated with many earthquake cycles involving individual segments. The irregularity of fault displacement data on timescales of 2–3 kyr revealed in this study demonstrates that observations on this timescale may not give results that are representative of the long-term evolution of this fault system. An analysis of variance showed that the shape of the slip profiles does not change for time periods of observation longer than 6 kyr. Application of methodologies presented here can determine over what timescales fault behaviour is fully sampled.
3. The distribution of displacement during the last 17 kyr along the Rangitaiki Fault system is largely controlled by relict segment boundaries that reflect the history of linkage of the fault system. The largest magnitude earthquakes have sufficient energy to rupture across these segment boundaries, whereas smaller magnitude events contribute to irregular surface displacement accumulation. We present a model for slip accumulation on a fault during repeated earthquakes in which larger events rupture the entire fault plane, with relatively smaller events having irregular slip profiles and failing to rupture across segments or asperities along the fault plane.

Acknowledgements

This work was funded by the Natural Environment Research Council (GR3/11862), United Kingdom and the New Zealand Foundation for Research Science and Technology (FRST-CO1X0038). We are grateful to the officers and crew of R/V

Tangaroa and R/V Kaharoa for their dedication during TAN-99-14 and KAH01-02, and to the technical team at NIWA for their expertise in geophysical data acquisition. The manuscript was improved by careful and constructive reviews from Gerald Roberts and Andy Nicol. Ian Wright is thanked for his support.

References

Aki, K., 1984. Asperities, barriers, characteristic earthquakes and strong motion prediction. Journal of Geophysical Research 89, 5867–5872.

Anderson, H.J., Webb, T.H., 1989. The rupture process of the Edgecumbe earthquake, New Zealand. New Zealand Journal of Geology and Geophysics 32, 43–52.

Anderson, H.J., Smith, E., Robinson, R., 1990. Normal faulting in a back-arc basin: seismological characteristics of the March 2, 1987, Edgecumbe, New Zealand, Earthquake. Journal of Geophysical Research 95, 4709–4723.

Beanland, S., Berryman, K.R., Blick, G.H., 1989. Geological investigations of the 1987 Edgecumbe earthquake, New Zealand. New Zealand Journal of Geology and Geophysics 32, 73–91.

Beanland, S., Blick, G.H., Darby, D.J., 1990. Normal faulting in a back-arc basin: geological and geodetic characteristics of the 1987 Edgecumbe earthquake, New Zealand. Journal of Geophysical Research 95, 4693–4707.

Bryan, C.J., Sherburn, S., Bibby, H.M., Bannister, S.C., Hurst, A.W., 1999. Shallow seismicity of the central Taupo Volcano Zone, New Zealand: its distribution and nature. New Zealand Journal of Geology and Geophysics 42, 533–542.

Carter, R.M., Carter, L., Johnson, D.P., 1986. Submergent shorelines, SW Pacific: episodic post-glacial transgression. Sedimentology 33, 629–649.

Chapman, T.J., Meneilly, A.W., 1991. The displacement patterns associated with a reverse-reactivated, normal growth fault. In: Roberts, A.M., Yielding, G., Freeman, B. (Eds.), The Geometry of Normal Faults Geological Society Special Publication 56, pp. 183–191.

Cowie, P.A., Scholz, C.H., 1992. Growth of faults by accumulation of seismic slip. Journal of Geophysical Research 97, 11085–11096.

Crone, A.J., Machette, M.N., 1984. Surface faulting accompanying the Borah Peak earthquake, central Idaho. Geology 12, 664–667.

Darby, D.J., 1989. Dislocation modelling of the 1987 Edgecumbe earthquake, New Zealand. New Zealand Journal of Geology and Geophysics 32, 115–122.

Davey, F.J., Henrys, S.A., Lodolo, E., 1995. Asymmetric rifting in a continental back-arc environment, North Island, New Zealand. Journal of Volcanological and Geothermal Research 68, 209–238.

Hanks, T.C., Kanamori, H., 1979. A moment magnitude scale. Journal of Geophysical Research 84, 2348–2350.

Hemphill-Haley, M.A., Weldon, R.J., 1999. Estimating prehistoric earthquake magnitude from point measurements of surface rupture. Bulletin of the Seismological Society of America 89, 1264–1279.

Kohn, B.P., Glasby, G.P., 1978. Tephra distribution and sedimentation rates in the Bay of Plenty, New Zealand. New Zealand Journal of Geology and Geophysics 21, 49–70.

Lamarche, G., Bull, J.M., Barnes, P.M., Taylor, S.K., Horgan, H., 2000. Constraining fault growth rates and fault evolution in New Zealand. Eos Transactions of the American Geophysical Union 81, 481–486.

Lamarche, G., Barnes, P.M., Bull, J.M., in press. Faulting and extension rate over the last 20,000 years in the Offshore Whakatane Graben, New Zealand Continental Shelf. Tectonics.

Manighetti, I., Campillo, M., Sammis, C., Mai, P.M., King, G., 2005. Evidence for self-similar, triangular slip distributions on earthquakes; implications for earthquake and fault mechanics. Journal of Geophysical Research 110, B05302. doi:10.1029/2004JB003174.

Mansfield, C.S., Cartwright, J.A., 1996. High-resolution displacement mapping from three-dimensional seismic data: evidence for dip linkage during fault growth. Journal of Structural Geology 18, 249–263.

Nairn, I.A., Beanland, S., 1989. Geological setting of the 1987 Edgecumbe earthquake, New Zealand. New Zealand Journal of Geology and Geophysics 32, 1–13.

Nicol, A., Walsh, J.J., Berryman, K., Nodder, S., 2005. Growth of a normal fault by the accumulation of slip over millions of years. Journal of Structural Geology 27, 541–551.

Peacock, D.C.P., Sanderson, D.J., 1996. Effects of propagation rate on displacement variations along faults. Journal of Structural Geology 18, 311–320.

Schwartz, D.P., 1989. Paleoseismicity, persistence of segments, and temporal clustering of large earthquakes—examples from the San Andreas, Wasatch, and lost River Fault Zones. In: Proceedings of Conference XLV, Fault Segmentation and Controls of Rupture Initiation and Termination. U.S. Geological Survey Open-file Report 89-315, pp. 361–375.

Schwartz, D.P., Coppersmith, K.J., 1984. Fault behavior and characteristic earthquakes: examples from the Wasatch and San Andreas Fault Zones. Journal of Geophysical Research 89, 5681–5698.

Sieh, K., Jones, L., Hauksson, E., Hudnut, K., Eberhart-Phillips, D., Heaton, T., Hough, S., Hutton, K., Kanamori, H., Lilje, A., Lindval, S., McGill, S.F., Mori, J., Rubin, C., Spotila, J.A., Stock, J., Thio, H., Treiman, J., Wernicke, B., Zachariasen, J., 1993. Near-field investigation of the Landers earthquake sequence, April to July, 1992. Science 260, 171–176.

Taylor, S.K., 2003. A long timescale high-resolution fault activity history of the Whakatane Graben, New Zealand. Ph.D. thesis, University of Southampton, UK.

Taylor, S.K., Bull, J.M., Lamarche, G., Barnes, P.M., 2004. Normal fault growth and linkage during the last 1.3 million years: an example from the Whakatane Graben, New Zealand. Journal of Geophysical Research 109, B02408. doi:10.1029/2003JB002412.

Villamor, P., Berryman, K., 2001. A late Quaternary extension rate in the Taupo Volcanic Zone, New Zealand, derived from fault slip data. New Zealand Journal of Geology and Geophysics 44, 243–269.

Wald, D.J., Heaton, T.H., 1994. Spatial and temporal distribution of slip for the 1992 Landers California Earthquake. Bulletin of the Seismological Society of America 84, 668–691.

Walsh, J.J., Watterson, J., 1988. Analysis of the relationship between displacements and dimensions of faults. Journal of Structural Geology. 10, 238–247.

Walsh, J.J., Watterson, J., 1991. Geometric and kinematic coherence and scale effects in normal fault systems. In: Roberts, A.M., Yielding, G., Freeman, B. (Eds.), The Geometry of Normal Faults Special Publication, Geological Society of London 56, pp. 193–203.

Wells, D.L., Coppersmith, K.J., 1994. New empirical relationships among magnitude, rupture length, rupture width, rupture area and surface displacement. Bulletin of the Seismological Society of America 84, 974–1002.

Wesnousky, S.G., 1986. Earthquakes, Quaternary faults and seismic hazard in California. Journal of Geophysical Research 91, 12587–12631.

Wright, I.C., 1990. Late Quaternary faulting of the offshore Whakatane Graben, Taupo Volcanic Zone, New Zealand. New Zealand Journal of Geology and Geophysics 33, 245–256.

Wright, T.J., Lu, Z., Wicks, C., 2004. Constraining the slip distribution and fault geometry of the M_w 7.9, 3 November 2002, Denali Fault earthquake with interferometric synthetic aperture radar and global positioning system data. Bulletin of the Seismological Society of America 94, S175–S189.